Runge Kutta explicit time integration-based discretize-then-optimize (DTO) modeling for dynamic force inversion

Stephen Lloyd[1] and Chanseok Jeong[2,3,4]

[1]Postdoctoral Researcher, School of Engineering and Technology, Central Michigan University, Mount Pleasant, MI 48859, USA.

[2]Associate Professor, School of Engineering and Technology, Central Michigan University, Mount Pleasant, MI 48859, USA (corresponding author).

[3]Member, Institute for Great Lakes Research, Central Michigan University, Mount Pleasant, MI 48859, USA.

[4]Member, Earth and Ecosystem Science Program, Central Michigan University, Mount Pleasant, MI 48859, USA.

Keywords— dynamic force inversion; Discretize-then-optimize; Runge-Kutta method; Moving loads.

ABSTRACT

This paper presents a new discretize-then-optimize (DTO) method for dynamic force inversion in a two-dimensional (2D) linear elastic, damped solid based on Runge-Kutta (RK) explicit time integration. Previous literature on DTO modeling for force or material inversion has predominantly focused on inversion methods based on Newmark implicit time integration. However, because implicit time integration may not be suitable for a problem with a large number of degrees of freedom (e.g., 3D wave problems), there is a need to study an alternative DTO force-inversion formulation that centers around the RK explicit time integration, leveraged by a diagonal mass matrix. This paper attempts to fill this gap and present the full detail of the new RK-DTO formulation for dynamic force inversion.

Our computational examples demonstrate that the new RK-DTO inversion simulator effectively reconstructs moving dynamic forces on the upper surface of the solid. It excels in efficiency when dealing with a higher number of degrees of freedom (DOFs) and maintains accuracy even with increased DOFs and observation durations. A smaller sensor spacing enhances the accuracy of the inverted force profile in the RK-based inversion. The presented inversion method can effectively identify the profiles of dynamic moving loads even when measurement data include noise or when the values of material properties are not deterministic.

INTRODUCTION

Dynamic force inversion is useful in a wide range of engineering applications, including (*i*) the identification of incoming seismic waves, which could be modeled as equivalent body forces, in a truncated domain (Guidio and Jeong 2021a; Guidio et al. 2022) and (*ii*) the inversion of moving dynamic forces in modern infrastructure (e.g., smart highways) (Jiang et al. 2003; Au et al. 2004; Jeong et al. 2017; Guidio and Jeong 2021b; Ni et al. 2023). Such inverse problems utilize dynamic motions that are measured by sparsely spaced sensors.

Partial differential equation (PDE)-constrained optimization allows for the estimation of a very large number of control parameters that discretize the unknown force over space and time. Thus, forces of any profile can be identified without prior information. PDE-constrained optimization requires the satisfaction of the first-order optimality conditions of a minimization functional, on which a PDE is side-imposed. Traditionally, a continuous form of PDE is side-imposed, and its adjoint and control equations are derived (via the variational method). Then, the continuous PDE of the adjoint equation is discretized, and solving the discretized adjoint problem constitutes the satisfaction of the optimal conditions. The order of this process is characterized as optimize-then-discretize (OTD).

On the other hand, in the DTO process, a PDE's discrete form is side imposed to the discrete form of a minimization functional, and the discrete adjoint and control problems are derived. The imposition of a PDE's discrete form, which is the actual physics solved by a numerical model, leads to the accurate evaluation of the gradient of a minimization functional by the numerical optimizer. As a primary merit of the DTO modeling, the DTO method allows more compact modeling than the OTD method even though the complex wave PDEs and boundary conditions are still considered.

The DTO procedure was utilized for characterizing wave sources in solids (Walsh et al. 2013). Lloyd and Jeong (2018) investigated the OTD modeling to identify the full profile of body force function in space and time in a 1D solid bar, and its DTO counterpart (Lloyd and Jeong 2022). The authors also tested DTO inverse modeling for the reconstruction of loads moving along the upper boundary of a 2D solid (Lloyd et al. 2023). Guidio and Jeong (2021a) also investigated both OTD and DTO for characterizing traction distribution in space and time in a 2D solid of anti-plane motion. Based on the proven robustness and compactness of the DTO modeling, Guidio et al. (2022) studied the DTO method for characterizing incoming seismic waves (modeled as traction on absorbing boundary conditions) in a truncated domain of SH wave motion. It should be noted that all the aforementioned DTO force inversion works are based on the Newmark implicit time integration as a forward operator. However, the implicit time integration may be less suitable than explicit time integration for a problem with a large number of DOFs (e.g., 3D wave problems) and large matrices. In such problems, the amount of time needed to complete all of the computations can be markedly large. While the implicit time integration uses the effective stiffness matrix, which cannot be diagonalized, the explicit time integration uses the inverse matrix of a diagonalized mass matrix, reducing the computation time. Thus, there is a need to study an alternative DTO force-inversion formulation that centers around the explicit time integration, taking advantage of a diagonal mass matrix. which could arise by virtue of the conventional finite element method (FEM) with mass lumping or spectral element method (SEM) (Komatitsch and Tromp 1999; Tromp et al. 2008).

This paper attempts to meet this need and present the full detail of the new DTO formulation for the force inversion using Runge-Kutta (RK) explicit time integration. The RK method has been used for computationally efficient forward modeling in problems that involve dynamic moving loads (Raftoyiannis et al. 2014; Lin and Trethewey 1990; Ding et al. 2012; Aloisio et al. 2022). To implement RK in the DTO modeling presented in this study, a forward operator models the RK explicit time integration and is side-imposed into a minimization functional via the multiplication with an adjoint solution vector. Details of how the adjoint problem of a discretized form is derived in the context of PDE-constrained optimization (i.e., the first-order optimality condition) and how the adjoint solver is implemented are discussed in this paper. Included in this discussion are how the gradient of the functional with respect to the discrete force parameter is derived in the DTO process, and how it is implemented in the numerical inversion solver. As an illustrative case, we examine a force-inversion scenario aimed at determining the patterns of dynamic loads that travels the upper boundary of a 2D solid.

To the merit of the presented RK-DTO formulation, it can be easily extended into various inverse problems (e.g., force inversion (Oh et al. 2023), inversion of incoming seismic waves (Jeong and Seylabi 2018; Ghahari et al. 2018a; Ghahari et al. 2018b), material characterization or geophysical inversion (Askan et al. 2007; Aguiló et al. 2010; Kallivokas et al. 2013; Pakravan et al. 2016), or inverse scattering (Jung et al. 2013; Jung and Taciroglu 2014; Jung and Taciroglu 2016; Chatzi et al. 2011; Guzina et al. 2003; Aquino et al. 2019)) in 2D/3D settings where the forward wave problems are solved by using the RK explicit time integration with diagonal mass matrices. Because the discreized forward operator, which already includes boundary conditions, heterogeneity, and anisotropy, is side-imposed into a minization functional, the presented method is scalable for various boundary conditions (e.g., absorbing boundary conditions) or material models.

PROBLEM DEFINITION

A 2D solid model (Fig. 1) of a rectangular shape with length, L, and height, H is employed to present the RK-DTO method. The solid is fixed at the lower boundary ($y = 0$). The model can have various configurations, including homogeneous or layered materials. It begins in a state of rest, and dynamic distributed forces may be applied to the upper surface ($y = H$). The side surfaces are not subject to traction. In numerical experiments conducted to test the presented inverse modeling approach, the loads applied to the top surface are the target loads to be reconstructed by the inverse model and can be moving or stationary. In the model, sensors at the top surface record vibrational motion data, including both x and y components of wave responses. The inverse model is evaluated using these sensor measurements in example cases. The presented dynamic force inversion method aims to minimize the difference between measured displacements and model displacements computed using predicted loads. Measured data may be acquired through the use of accelerometers, distributed acoustic sensors (DAS) (Daley et al. 2013), or vision-based motion sensors (Ngeljaratan and Moustafa 2020). In this computational study, synthetic measurement data, created via wave simulations, are utilized. The solution of wave motions is numerically obtained via the FEM and the RK explicit time integration. Then, a new DTO modeling is examined for the force inversion that includes the side imposition of the forward operator in the discrete form, the derivation of the discrete adjoint equation, and the implementation of the adjoint equation.

Governing wave physics

The plane-strain setting for 2D models is used in this study, and the wave motion in the domain Ω is governed by:

$$\nabla \cdot \boldsymbol{\sigma} - \alpha \dot{\mathbf{u}} = \rho \ddot{\mathbf{u}} \quad \text{in } \Omega, \tag{1}$$

where $\boldsymbol{\sigma}$ denotes the stress tensor, α denotes a damping coefficient, ρ is the mass density, and $\mathbf{u} = [u_x, u_y]$ represents the displacements. The moving loads applied, on the upper surface, are distributed forces $\boldsymbol{\sigma}\mathbf{n} = [f_x(x,t); f_y(x,t)]$, where $f_x(x,t)$ and $f_y(x,t)$ denote traction functions for $0 \leq x \leq L$ and $0 \leq t \leq T$, and $\mathbf{n}$ denotes the outward normal unit vector on the boundaries.

It should be noted that while the boundary conditions for the model in this study represent a specific case, our DTO inversion can model various other boundary conditions, such as wave-absorbing boundary conditions, to model the large extent of transportation infrastructure, like perfectly-matched-layers (Fathi et al. 2015; Kucukcoban and Kallivokas 2011) and consistent transmitting boundaries (Lee 2023).

FORWARD MODELING

The numerical solution of the wave motion is obtained through the Galerkin FEM. In previous force-inversion research (Lloyd and Jeong 2018; Lloyd and Jeong 2022; Lloyd et al. 2023), the Newmark time integration scheme was used to compute displacements at discrete time steps. However, this study focuses on the RK method to compute displacements at each discrete time step. Because of the ease of inverting a diagonal mass matrix, the RK method generally requires less computational time than the Newmark method when the number of the time steps are equal to each other. The computational efficiency of the RK time integration, relative to the Newmark time integration, becomes increasingly significant for larger models. However, for the given finite element mesh, convergence using the RK method is conditional based on the time step size. It is selected to satisfy the following Courant-Friedrichs-Lewy (CFL) condition for convergence, useful for explicit time integration schemes, $\mathcal{C} = \frac{v_{max}(\Delta t)}{r_{min}} \leq \mathcal{C}_{max}$, where $\mathcal{C}$ is the Courant number; v_{max}

is the largest wave speed of the material(s) used in the model; Δt is the time step size; r_{min} is smallest distance between nodes in the finite element model, and it decreases as the frequency of wave increases; and $\mathcal{C}_{max}$ is the maximum allowable Courant number, typically equal to one. Choosing $\mathcal{C}_{max} = 1$, the time steps used in this study meet the following condition, $\Delta t \leq \frac{r_{min}}{v_{max}}$.

The wave equation (1) for the solid can be expressed in a matrix form, by virtue of the finite element approximation, as:

$$\mathbf{K}\mathbf{s}(t) + \mathbf{C}\dot{\mathbf{s}}(t) + \mathbf{M}\ddot{\mathbf{s}}(t) = \mathbf{f}(t), \tag{2}$$

where $\mathbf{s}(t) = [\mathbf{u}_x(t); \mathbf{u}_y(t)]$; $\mathbf{u}_x(t)$ and $\mathbf{u}_y(t)$ are the solution vectors in all nodes at time t; and $\mathbf{K}$, $\mathbf{C}$, and $\mathbf{M}$ are the global stiffness, damping, and mass matrices. The element mass matrices are numerically integrated in each element by using the conventional Gauss quadrature and diagonalized by using the mass lumping technique. While letting $\mathbf{y}(t) = \dot{\mathbf{s}}(\mathbf{t})$, the discrete form, Eq. (2), is multiplied through by $\mathbf{M}^{-1}$ such that:

$$-\mathbf{y}(t) + \dot{\mathbf{s}}(\mathbf{t}) = 0 \tag{3}$$

$$\mathbf{M}^{-1}\mathbf{K}\mathbf{s}(t) + \mathbf{M}^{-1}\mathbf{C}\underbrace{\dot{\mathbf{s}}(t)}_{\mathbf{y}(t)} + \underbrace{\ddot{\mathbf{s}}(t)}_{\dot{\mathbf{y}}(\mathbf{t})} = \mathbf{M}^{-1}\mathbf{f}(t). \tag{4}$$

The discrete form equations (3) and (4) can be rearranged so that the derivatives of $\mathbf{s}(t)$ and $\mathbf{y}(t)$ over time are alone on the left side of the equation gives:

$$\dot{\overline{\mathbf{s}}}(t) = \mathbf{J}\overline{\mathbf{s}}(t) + \underline{\mathbf{M}}^{-1}\overline{\mathbf{f}}(t), \tag{5}$$

where

$$\overline{\mathbf{s}}(t) = \begin{bmatrix} \mathbf{s}(t) \\ \mathbf{y}(t) \end{bmatrix}, \quad \dot{\overline{\mathbf{s}}}(t) = \begin{bmatrix} \dot{\mathbf{s}}(t) \\ \dot{\mathbf{y}}(t) \end{bmatrix}, \tag{6}$$

$$\mathbf{J} = -\begin{bmatrix} \mathbf{0} & -\mathbf{I} \\ \mathbf{M}^{-1}\mathbf{K} & \mathbf{M}^{-1}\mathbf{C} \end{bmatrix}, \quad \underline{\mathbf{M}}^{-1} = \begin{bmatrix} \mathbf{I} & \mathbf{0} \\ \mathbf{0} & \mathbf{M}^{-1} \end{bmatrix}, \quad \overline{\mathbf{f}}(t) = \begin{bmatrix} \mathbf{0} \\ \mathbf{f}(t) \end{bmatrix}. \tag{7}$$

For every discrete n-th time step, equation (5) can be written:

$$\dot{\overline{\mathbf{s}}}_n = \mathbf{J}\overline{\mathbf{s}}_n + \underline{\mathbf{M}}^{\mathbf{-1}}\overline{\mathbf{f}}_n. \tag{8}$$

The initial displacements and velocities are zero $\overline{\mathbf{s}}_0 = 0$, and

$$\dot{\overline{\mathbf{s}}}_0 = \mathbf{J}\overline{\mathbf{s}}_0 + \underline{\mathbf{M}}^{-1}\overline{\mathbf{f}}_0 = \begin{bmatrix} \mathbf{0} \\ \mathbf{M}^{-1}\mathbf{f}(t=0) \end{bmatrix}. \tag{9}$$

Using the fourth-order RK method, the vector $\overline{\mathbf{s}}_n$ is computed each n-th time step, after the initial time, with following equation:

$$\overline{\mathbf{s}}_n = \overline{\mathbf{s}}_{n-1} + \Delta t \frac{1}{6}\left(\mathbf{k}_1 + 2\mathbf{k}_2 + 2\mathbf{k}_3 + \mathbf{k}_4\right), \tag{10}$$

where

$$\mathbf{k}_1 = \frac{\partial \overline{\mathbf{s}}}{\partial t}\left(t_{n-1}, \overline{\mathbf{s}}_{n-1}\right) = \mathbf{J}\overline{\mathbf{s}}_{n-1} + \underline{\mathbf{M}}^{-1}\overline{\mathbf{f}}_{n-1}, \tag{11}$$

$$\mathbf{k}_2 = \frac{\partial \overline{\mathbf{s}}}{\partial t}\left(t_{n-1} + \frac{\Delta t}{2}, \overline{\mathbf{s}}_{n-1} + \frac{\Delta t}{2}\mathbf{k}_1\right) = \mathbf{J}\left(\overline{\mathbf{s}}_{n-1} + \frac{\Delta t}{2}\mathbf{k}_1\right) + \underline{\mathbf{M}}^{-1}\overline{\mathbf{f}}_{n-0.5}, \tag{12}$$

$$\mathbf{k}_3 = \frac{\partial \overline{\mathbf{s}}}{\partial t}\left(t_{n-1} + \frac{\Delta t}{2}, \overline{\mathbf{s}}_{n-1} + \frac{\Delta t}{2}\mathbf{k}_2\right) = \mathbf{J}\left(\overline{\mathbf{s}}_{n-1} + \frac{\Delta t}{2}\mathbf{k}_2\right) + \underline{\mathbf{M}}^{-1}\overline{\mathbf{f}}_{n-0.5}, \tag{13}$$

$$\mathbf{k}_4 = \frac{\partial \overline{\mathbf{s}}}{\partial t}\left(t_n, \overline{\mathbf{s}}_{n-1} + \Delta t\mathbf{k}_3\right) = \mathbf{J}\left(\overline{\mathbf{s}}_{n-1} + \Delta t\mathbf{k}_3\right) + \underline{\mathbf{M}}^{-1}\overline{\mathbf{f}}_n, \tag{14}$$

and

$$\underline{\mathbf{M}}^{-1}\overline{\mathbf{f}}_{n-0.5} = \begin{bmatrix} \mathbf{0} \\ \mathbf{M}^{-1}\mathbf{f}\left(t = t_{n-1} + \frac{\Delta t}{2}\right) \end{bmatrix}. \tag{15}$$

By expressing $\mathbf{k}_1$, $\mathbf{k}_2$, $\mathbf{k}_3$, and $\mathbf{k}_4$ in terms of $\overline{\mathbf{s}}_{n-1}$, $\overline{\mathbf{f}}_{n-1}$, $\overline{\mathbf{f}}_{n-0.5}$, and $\overline{\mathbf{f}}_n$ and substituting $\mathbf{k}_1$, $\mathbf{k}_2$, $\mathbf{k}_3$, and $\mathbf{k}_4$ into the RK method, Eq. (10) results in the following RK method equation written in terms of $\bar{\mathbf{s}}_{n-1}$, $\bar{\mathbf{f}}_{n-1}$, $\bar{\mathbf{f}}_{n-0.5}$, and $\bar{\mathbf{f}}_n$:

$$\bar{\mathbf{s}}_n = \bar{\mathbf{s}}_{n-1} + \frac{\Delta t}{6}\left(\mathbf{J} + 2\mathbf{L}_1 + 2\mathbf{L}_3 + \mathbf{L}_6\right)\bar{\mathbf{s}}_{n-1} + \frac{\Delta t}{6}\left(\mathbf{I} + 2\mathbf{L}_2 + 2\mathbf{L}_4 + \mathbf{L}_7\right)\underline{\mathbf{M}}^{-1}\bar{\mathbf{f}}_{n-1}$$
$$+ \frac{\Delta t}{6}\left(2\mathbf{I} + 2\mathbf{L}_5 + \mathbf{L}_8\right)\underline{\mathbf{M}}^{-1}\bar{\mathbf{f}}_{n-0.5} + \frac{\Delta t}{6}\underline{\mathbf{M}}^{-1}\bar{\mathbf{f}}_n, \tag{16}$$

where

$$\mathbf{L}_1 = \mathbf{J} + \frac{\Delta t}{2}\mathbf{J}\mathbf{J}, \quad \mathbf{L}_2 = \frac{\Delta t}{2}\mathbf{J}, \tag{17}$$
$$\mathbf{L}_3 = \mathbf{J} + \frac{\Delta t}{2}\mathbf{J}\mathbf{L}_1, \quad \mathbf{L}_4 = \frac{\Delta t}{2}\mathbf{J}\mathbf{L}_2, \tag{18}$$
$$\mathbf{L}_5 = \frac{\Delta t}{2}\mathbf{J} + \mathbf{I}, \quad \mathbf{L}_6 = \mathbf{J} + \Delta t\mathbf{J}\mathbf{L}_3, \tag{19}$$
$$\mathbf{L}_7 = \Delta t\mathbf{J}\mathbf{L}_4, \quad \mathbf{L}_8 = \Delta t\mathbf{J}\mathbf{L}_5. \tag{20}$$

Appendix I shows a detailed description of deriving $\mathbf{L}_1$ to $\mathbf{L}_8$ by expressing $\mathbf{k}_1$, $\mathbf{k}_2$, $\mathbf{k}_3$, and $\mathbf{k}_4$ in terms of $\bar{\mathbf{s}}_{n-1}$, $\bar{\mathbf{f}}_{n-1}$, $\bar{\mathbf{f}}_{n-0.5}$, and $\bar{\mathbf{f}}_n$. The RK method equation (16) can be written even more compactly:

$$\bar{\mathbf{s}}_n - \bar{\mathbf{s}}_{n-1} - \mathbf{A}_1\bar{\mathbf{s}}_{n-1} - \mathbf{A}_2\bar{\mathbf{f}}_{n-1} - \mathbf{A}_3\bar{\mathbf{f}}_{n-0.5} - \mathbf{A}_4\bar{\mathbf{f}}_n = 0, \tag{21}$$

where

$$\mathbf{A}_1 = \frac{\Delta t}{6}\left(\mathbf{J} + 2\mathbf{L}_1 + 2\mathbf{L}_3 + \mathbf{L}_6\right), \tag{22}$$
$$\mathbf{A}_2 = \frac{\Delta t}{6}\left(\mathbf{I} + 2\mathbf{L}_2 + 2\mathbf{L}_4 + \mathbf{L}_7\right)\underline{\mathbf{M}}^{-1}, \tag{23}$$
$$\mathbf{A}_3 = \frac{\Delta t}{6}\left(2\mathbf{I} + 2\mathbf{L}_5 + \mathbf{L}_8\right)\underline{\mathbf{M}}^{-1}, \tag{24}$$
$$\mathbf{A}_4 = \frac{\Delta t}{6}\underline{\mathbf{M}}^{-1}. \tag{25}$$

The RK method can now be shown in the compact equation:

$$\mathbf{Q}\hat{\mathbf{s}} - \mathbf{R}\hat{\mathbf{f}} = 0, \tag{26}$$

where $\hat{\mathbf{s}}$ and $\hat{\mathbf{f}}$ are constructed for each time step as follows:

$$\hat{\mathbf{s}} = \begin{bmatrix} \bar{\mathbf{s}}_0 \\ \mathbf{0} \\ \bar{\mathbf{s}}_1 \\ \mathbf{0} \\ \bar{\mathbf{s}}_2 \\ \mathbf{0} \\ \vdots \\ \bar{\mathbf{s}}_{N-1} \\ \mathbf{0} \\ \bar{\mathbf{s}}_N \end{bmatrix}, \quad \hat{\mathbf{f}} = \begin{bmatrix} \bar{\mathbf{f}}_0 \\ \bar{\mathbf{f}}_{0.5} \\ \bar{\mathbf{f}}_1 \\ \bar{\mathbf{f}}_{1.5} \\ \bar{\mathbf{f}}_2 \\ \bar{\mathbf{f}}_{2.5} \\ \vdots \\ \bar{\mathbf{f}}_{N-1} \\ \bar{\mathbf{f}}_{N-0.5} \\ \bar{\mathbf{f}}_N \end{bmatrix}, \tag{27}$$

where N is the final time step. The vectors $\bar{\mathbf{f}}_0$ to $\bar{\mathbf{f}}_N$ are subvectors of the vector $\hat{\mathbf{f}}$ and contain zeros and forces at every node ordered as in equation (7) at each half time step. The vectors $\bar{\mathbf{s}}_0$ to $\bar{\mathbf{s}}_N$ are subvectors of the vector $\hat{\mathbf{s}}$ and contain the displacements and velocities at every node ordered as in equation (6) at each full time step. Displacements and velocities at the half time steps are not needed to solve the RK method equation (21), so the subvectors for the half time steps in $\hat{\mathbf{s}}$ are treated as zero vectors. There are x- and y-components of displacement, velocity and force so the $\bar{\mathbf{s}}$ and $\bar{\mathbf{f}}$ subvectors each have the dimension $2(2j_N) \times 1$ where j_N is the number of nodes except for those with Dirichlet boundary conditions. Since there are subvectors in $\hat{\mathbf{s}}$ and $\hat{\mathbf{f}}$ for the initial step, each half time step, and each full time step, there are $2N+1$ subvectors. Thus, $\hat{\mathbf{s}}$ and $\hat{\mathbf{f}}$ each have the dimensions of $2(2j_N)(2N+1)\times 1$. The matrix $\mathbf{Q}$ is defined as:

$$\mathbf{Q} = \begin{bmatrix} \mathbf{I} & \mathbf{0} & \mathbf{0} & \mathbf{0} & \mathbf{0} & \mathbf{0} & \dots & \mathbf{0} & \mathbf{0} & \mathbf{0} \\ \mathbf{0} & \mathbf{0} & \mathbf{0} & \mathbf{0} & \mathbf{0} & \mathbf{0} & \dots & \mathbf{0} & \mathbf{0} & \mathbf{0} \\ -\mathbf{I}-\mathbf{A}_1 & \mathbf{0} & \mathbf{I} & \mathbf{0} & \mathbf{0} & \mathbf{0} & \dots & \mathbf{0} & \mathbf{0} & \mathbf{0} \\ \mathbf{0} & \mathbf{0} & \mathbf{0} & \mathbf{0} & \mathbf{0} & \mathbf{0} & \dots & \mathbf{0} & \mathbf{0} & \mathbf{0} \\ \mathbf{0} & \mathbf{0} & -\mathbf{I}-\mathbf{A}_1 & \mathbf{0} & \mathbf{I} & \mathbf{0} & \dots & \mathbf{0} & \mathbf{0} & \mathbf{0} \\ \mathbf{0} & \mathbf{0} & \mathbf{0} & \mathbf{0} & \mathbf{0} & \mathbf{0} & \dots & \mathbf{0} & \mathbf{0} & \mathbf{0} \\ \vdots & \vdots & \vdots & \vdots & \vdots & \vdots & \ddots & \vdots & \vdots & \vdots \\ \mathbf{0} & \mathbf{0} & \mathbf{0} & \mathbf{0} & \mathbf{0} & \mathbf{0} & \dots & \mathbf{I} & \mathbf{0} & \mathbf{0} \\ \mathbf{0} & \mathbf{0} & \mathbf{0} & \mathbf{0} & \mathbf{0} & \mathbf{0} & \dots & \mathbf{0} & \mathbf{0} & \mathbf{0} \\ \mathbf{0} & \mathbf{0} & \mathbf{0} & \mathbf{0} & \mathbf{0} & \mathbf{0} & \dots & -\mathbf{I}-\mathbf{A}_1 & \mathbf{0} & \mathbf{I} \end{bmatrix}. \tag{28}$$

The matrix $\mathbf{R}$ is defined as:

$$\mathbf{R} = \begin{bmatrix} \mathbf{0} & \mathbf{0} & \mathbf{0} & \mathbf{0} & \mathbf{0} & \mathbf{0} & \dots & \mathbf{0} & \mathbf{0} & \mathbf{0} \\ \mathbf{0} & \mathbf{0} & \mathbf{0} & \mathbf{0} & \mathbf{0} & \mathbf{0} & \dots & \mathbf{0} & \mathbf{0} & \mathbf{0} \\ \mathbf{A}_2 & \mathbf{A}_3 & \mathbf{A}_4 & \mathbf{0} & \mathbf{0} & \mathbf{0} & \dots & \mathbf{0} & \mathbf{0} & \mathbf{0} \\ \mathbf{0} & \mathbf{0} & \mathbf{0} & \mathbf{0} & \mathbf{0} & \mathbf{0} & \dots & \mathbf{0} & \mathbf{0} & \mathbf{0} \\ \mathbf{0} & \mathbf{0} & \mathbf{A}_2 & \mathbf{A}_3 & \mathbf{A}_4 & \mathbf{0} & \dots & \mathbf{0} & \mathbf{0} & \mathbf{0} \\ \mathbf{0} & \mathbf{0} & \mathbf{0} & \mathbf{0} & \mathbf{0} & \mathbf{0} & \dots & \mathbf{0} & \mathbf{0} & \mathbf{0} \\ \vdots & \vdots & \vdots & \vdots & \vdots & \vdots & \ddots & \vdots & \vdots & \vdots \\ \mathbf{0} & \mathbf{0} & \mathbf{0} & \mathbf{0} & \mathbf{0} & \mathbf{0} & \dots & \mathbf{A}_4 & \mathbf{0} & \mathbf{0} \\ \mathbf{0} & \mathbf{0} & \mathbf{0} & \mathbf{0} & \mathbf{0} & \mathbf{0} & \dots & \mathbf{0} & \mathbf{0} & \mathbf{0} \\ \mathbf{0} & \mathbf{0} & \mathbf{0} & \mathbf{0} & \mathbf{0} & \mathbf{0} & \dots & \mathbf{A}_2 & \mathbf{A}_3 & \mathbf{A}_4 \end{bmatrix}. \tag{29}$$

The $\mathbf{Q}$ and $\mathbf{R}$ matrices have the same order, $2(2j_N)(2N+1)\times 2(2j_N)(2N+1)$.

INVERSE MODELING

To reconstruct wave sources, guessed loads are iteratively estimated to minimize the misfit between the measured motions and the model wave responses that are computed by the forward model when the guessed loads are applied.

Discrete objective and Lagrangian functionals

The continuous form of the objective functional to be minimized is:

$$\mathcal{L} = \int_0^T \sum_{q=1}^{q_N} (\mathbf{u}_{\mathrm{m}_q} - \mathbf{u}_q) \cdot (\mathbf{u}_{\mathrm{m}_q} - \mathbf{u}_q) dt, \tag{30}$$

where $\mathbf{u}_{\mathrm{m}_q}$ is the displacement recorded at the q-th measurement point, $\mathbf{u}_q$ is its calculated counterpart at the same location induced by guessed force, and q_N is the total number of measurement points. Equation (30) is rewritten with the temporal integration in the discrete fashion:

$$\hat{\mathcal{L}} = (\hat{\mathbf{s}}_{\mathrm{m}} - \hat{\mathbf{s}})^T \underline{\mathbf{B}} (\hat{\mathbf{s}}_{\mathrm{m}} - \hat{\mathbf{s}}), \tag{31}$$

where $\hat{\mathbf{s}}_m$ is the vector, which contains measured displacements and velocities at sensors and discrete points in time, and $\hat{\mathbf{s}}$ is the vector of discrete displacements and velocities calculated using the forward model and the guessed loading. The matrix, $\underline{\mathbf{B}}$, is a block diagonal matrix with $\underline{\mathbf{B}}_{\mathbf{s}}$ on the diagonal:

$$\underline{\mathbf{B}} = \begin{bmatrix} \underline{\mathbf{B}}_{\mathbf{s}} & \mathbf{0} & \mathbf{0} & \dots & \mathbf{0} & \mathbf{0} & \mathbf{0} \\ \mathbf{0} & \mathbf{0} & \mathbf{0} & \dots & \mathbf{0} & \mathbf{0} & \mathbf{0} \\ \mathbf{0} & \mathbf{0} & \underline{\mathbf{B}}_{\mathbf{s}} & \dots & \mathbf{0} & \mathbf{0} & \mathbf{0} \\ \vdots & \vdots & \vdots & \ddots & \vdots & \vdots & \vdots \\ \mathbf{0} & \mathbf{0} & \mathbf{0} & \dots & \underline{\mathbf{B}}_{\mathbf{s}} & \mathbf{0} & \mathbf{0} \\ \mathbf{0} & \mathbf{0} & \mathbf{0} & \dots & \mathbf{0} & \mathbf{0} & \mathbf{0} \\ \mathbf{0} & \mathbf{0} & \mathbf{0} & \dots & \mathbf{0} & \mathbf{0} & \underline{\mathbf{B}}_{\mathbf{s}} \end{bmatrix}, \tag{32}$$

where

$$\underline{\mathbf{B}}_{\mathbf{s}} = \begin{bmatrix} \Delta t \mathbf{B} & \mathbf{0} \\ \mathbf{0} & \mathbf{0} \end{bmatrix}, \tag{33}$$

corresponding to

$$\bar{\mathbf{s}}_n = \begin{bmatrix} \mathbf{s}_n \\ \dot{\mathbf{s}}_n \end{bmatrix}. \tag{34}$$

The matrix $\mathbf{B}$ contains ones along its diagonal elements, which correspond to the horizontal and vertical components of the nodes where sensors are positioned, while all other elements are zeros. The configuration of $\underline{\mathbf{B}}$ leads to the comparison of measured and computed displacements at sensor locations being the basis for the determination of the misfit using the discrete objective functional, Eq. (31). Even though the RK-based forward model computes velocities of particle motions at each time step, the velocities are not considered in the objective functional in this work. Of course, the velocities $\dot{\mathbf{s}}_n$ can potentially be considered in the objective functional by using the following:

$$\underline{\mathbf{B}}_{\mathbf{s}} = \begin{bmatrix} \mathbf{0} & \mathbf{0} \\ \mathbf{0} & \Delta t \mathbf{B} \end{bmatrix}. \tag{35}$$

In tests of the inversion method that include velocities in the object functional, it has been observed that the inversion is much slower in terms of the number of iterations to achieve the same value of the error norm per Eq. (50) than using just displacements. It is observed that the final inversion accuracy is about the same for both displacement and velocity measurement-based approaches, and only the displacements-based approach is used in the presented numerical examples.

Imposing Eq. (26), which is the compact expression of the considered RK time integration, which arises after the global assembly of element matrices, onto the discrete objective functional using a Lagrange multiplier $\hat{\boldsymbol{\lambda}}^T$ gives the following discrete Lagrangian functional:

$$\hat{\mathcal{A}} = (\hat{\mathbf{s}}_m - \hat{\mathbf{s}})^T \underline{\mathbf{B}} (\hat{\mathbf{s}}_m - \hat{\mathbf{s}}) - \hat{\boldsymbol{\lambda}}^T \left(\mathbf{Q}\hat{\mathbf{s}} - \mathbf{R}\hat{\mathbf{f}} \right), \tag{36}$$

where $\hat{\boldsymbol{\lambda}}^T = \begin{bmatrix} \boldsymbol{\lambda}_{\mathbf{0}}{}^T & \mathbf{0} & \boldsymbol{\lambda}_1{}^T & \mathbf{0} & \dots & \boldsymbol{\lambda}_{N-1}{}^T & \mathbf{0} & \boldsymbol{\lambda}_N{}^T \end{bmatrix}$. The vector, $\hat{\boldsymbol{\lambda}}^T$, has the order $1 \times 2(2j_N)(2N+1)$. Like $\hat{\mathbf{s}}$, $\hat{\boldsymbol{\lambda}}^T$ contains subvectors that represent components at each time step with zero vectors for subvectors at the half time steps.

The first-order optimality conditions

The gradient of the objective functional is used to iteratively update guessed forces for all spatial and temporal points in a given problem. To determine the gradient of the objective functional each inversion iteration, the following optimality conditions are applied to the Lagrangian functional, Eq. (36):

$$\frac{\partial \hat{\mathcal{A}}}{\partial \hat{\boldsymbol{\lambda}}} = 0, \quad \frac{\partial \hat{\mathcal{A}}}{\partial \hat{\mathbf{s}}} = 0, \quad \frac{\partial \hat{\mathcal{A}}}{\partial \hat{\mathbf{f}}} = 0. \tag{37}$$

The first optimality condition

Taking the partial derivative of the Lagrangian functional, Eq. (36), over the Lagrange variable, $\hat{\boldsymbol{\lambda}}$, and the optimality condition is satisfied since the discrete forward problem, Eq. (26), is resolved by our forward wave solver:

$$\frac{\partial \hat{\mathcal{A}}}{\partial \hat{\boldsymbol{\lambda}}} = -\mathbf{Q}\hat{\mathbf{s}} + \mathbf{R}\hat{\mathbf{f}} = 0. \tag{38}$$

The second optimality condition

Enforcing the condition that the partial derivative of $\hat{\mathcal{A}}$ with respect to the state solution $\hat{\mathbf{s}}$ must vanish reveals the adjoint equation in the discrete form to be:

$$\frac{\partial \hat{\mathcal{A}}}{\partial \hat{\mathbf{s}}} = \underbrace{2\underline{\mathbf{B}}(\hat{\mathbf{s}} - \hat{\mathbf{s}}_m) - \mathbf{Q}^T \hat{\boldsymbol{\lambda}} = 0}_{\text{discrete adjoint equation}}, \tag{39}$$

where $\mathbf{Q}^T$ is as follows:

$$\mathbf{Q}^T = \begin{bmatrix} \mathbf{I} & \mathbf{0} & (-\mathbf{I}-\mathbf{A}_1)^T & \mathbf{0} & \mathbf{0} & \mathbf{0} & \dots & \mathbf{0} & \mathbf{0} & \mathbf{0} \\ \mathbf{0} & \mathbf{0} & \mathbf{0} & \mathbf{0} & \mathbf{0} & \mathbf{0} & \dots & \mathbf{0} & \mathbf{0} & \mathbf{0} \\ \mathbf{0} & \mathbf{0} & \mathbf{I} & \mathbf{0} & (-\mathbf{I}-\mathbf{A}_1)^T & \mathbf{0} & \dots & \mathbf{0} & \mathbf{0} & \mathbf{0} \\ \mathbf{0} & \mathbf{0} & \mathbf{0} & \mathbf{0} & \mathbf{0} & \mathbf{0} & \dots & \mathbf{0} & \mathbf{0} & \mathbf{0} \\ \mathbf{0} & \mathbf{0} & \mathbf{0} & \mathbf{0} & \mathbf{0} & \mathbf{0} & \dots & \mathbf{0} & \mathbf{0} & \mathbf{0} \\ \mathbf{0} & \mathbf{0} & \mathbf{0} & \mathbf{0} & \mathbf{I} & \mathbf{0} & \dots & \mathbf{0} & \mathbf{0} & \mathbf{0} \\ \vdots & \vdots & \vdots & \vdots & \vdots & \vdots & \ddots & \vdots & \vdots & \vdots \\ \mathbf{0} & \mathbf{0} & \mathbf{0} & \mathbf{0} & \mathbf{0} & \mathbf{0} & \dots & \mathbf{I} & \mathbf{0} & (-\mathbf{I}-\mathbf{A}_1)^T \\ \mathbf{0} & \mathbf{0} & \mathbf{0} & \mathbf{0} & \mathbf{0} & \mathbf{0} & \dots & \mathbf{0} & \mathbf{0} & \mathbf{0} \\ \mathbf{0} & \mathbf{0} & \mathbf{0} & \mathbf{0} & \mathbf{0} & \mathbf{0} & \dots & \mathbf{0} & \mathbf{0} & \mathbf{I} \end{bmatrix}. \tag{40}$$

The derivation of the discrete adjoint equation is straightforward so it is not shown in this paper (the background of the derivation of the discrete adjoint problem is detailed by Guidio et al. (2022)). $\boldsymbol{\lambda}_n$ can be determined for each time step in reverse order starting from the final time step, $n = N$:

$$\boldsymbol{\lambda}_N = 2\underline{\mathbf{B}}_{\mathbf{s}}(\mathbf{s}_N - \mathbf{s}_{m_N}). \tag{41}$$

For time steps $n = N-1, N-2 \dots 0$, this work computes:

$$\boldsymbol{\lambda}_n = 2\underline{\mathbf{B}}_{\mathbf{s}}(\mathbf{s}_n - \mathbf{s}_{m_n}) - (-\mathbf{I}-\mathbf{A}_1)^T\boldsymbol{\lambda}_{n+1}. \tag{42}$$

Namely, the adjoint solver is straightforwardly implemented via equations (41) and (42).

The third optimality condition

The partial derivative of $\hat{\mathcal{A}}$ over $\hat{\mathbf{f}}$ is:

$$\frac{\partial\hat{\mathcal{A}}}{\partial\hat{\mathbf{f}}} = \mathbf{R}^T\hat{\boldsymbol{\lambda}}. \tag{43}$$

The gradient of $\hat{\mathcal{L}}$ over the control parameter vector, $\hat{\mathbf{f}}$, for all points in space in time can be evaluated as:

$$\hat{\mathbf{g}} = \mathbf{R}^T \hat{\boldsymbol{\lambda}}, \tag{44}$$

where $\hat{\mathbf{g}}$ has the order $2(2j_N)(2N+1) \times 1$, the same order as $\hat{\mathbf{f}}$, and contains gradient values for all points in space and time (including even half time steps that are required in the RK forward modeling).

The parameter-updating scheme

The estimated force is updated via the conjugate gradient method as follows:

$$\hat{\mathbf{f}}_{i+1} = \hat{\mathbf{f}}_i + h_i \hat{\mathbf{d}}_i, \tag{45}$$

where $\hat{\mathbf{f}}_i$ represents the estimated load at the i-th iteration, h_i signifies a step size, and $\hat{\mathbf{d}}_i$ denotes the search direction, determined through the subsequent conjugate-gradient computation: for $i = 0$ and every 50-th iteration, $\hat{\mathbf{d}}_i = -\hat{\mathbf{g}}_i$, and for $i \geq 1$ except every 50-th iteration, $\hat{\mathbf{d}}_i = -\hat{\mathbf{g}}_i + \frac{\hat{\mathbf{g}}_i \cdot \hat{\mathbf{g}}_i}{\hat{\mathbf{g}}_{i-1} \cdot \hat{\mathbf{g}}_{i-1}} \hat{\mathbf{d}}_{i-1}$. Thus, the search direction is reset at every 50-th iteration to $-\hat{\mathbf{g}}_i$ to avoid errors potentially accumulated over the iterations of calculating the search direction (Kang and Kallivokas 2010).

Assuming that the target load is reasonably situated on the solid's upper surface, equation (45) for parameter updates can be adjusted to modify the guessed loading exclusively at surface nodes rather than every node throughout the solid domain. The modified parameter update equation is the following:

$$\hat{\mathbf{f}}_{i+1} = \hat{\mathbf{f}}_i + h_i \mathbf{D} \hat{\mathbf{d}}_i. \tag{46}$$

Herein $\mathbf{D}$ represents a diagonal matrix with ones at its diagonal elements corresponding to nodes situated on the upper surface and zeros elsewhere. It was found in a previous investigation of Newmark-based moving-force inversion (Lloyd et al. 2023) that updating the guessed forces at the top surface of the solid, as in equation (46), yields more accurate results than determining the guessed forces at all nodal points in the solid. The ideal step size h_i, which corresponds to the one causing the greatest reduction in the objective functional upon updating the estimated load, is calculated using Newton's scheme as detailed by Lloyd and Jeong (2018). Parameter updating is stopped if the total number of iterations reaches a limit (e.g., 300). Alternatively, it can be stopped if the value of the misfit functional, $\hat{\mathcal{L}}$, at a given iteration decreases less than 1% of that at a previous iteration over three consecutive times.

NUMERICAL EXPERIMENTS

This paper compares the performance of the inversion algorithm for reconstructing moving loads using the RK forward simulation with that of the reference algorithm using the Newmark forward simulation. In each numerical experiment, moving loads serve as target loads to reconstruct. The FEM models in the numerical experiments use 9-node square, quadratic elements of an element size of 1 m. Using equation (46), it is assumed that the y-position of all moving loads is known to be at the top surface of the solid prior to beginning the reconstruction of the loading.

However, all other information about the target—e.g., the distributions of $f_x(x, H, t)$ and $f_y(x, H, t)$ over space and time—is unknown prior to reconstruction. An initial guess is $\hat{\mathbf{f}}_0 = 0$, i.e., the components of force in all space and time are initially predicted to be zero.

Targeted dynamic forces

The targeted moving loads, for $0 \leq t \leq T$, are defined as:

$$f_x(x, H, t) = \sum_{k=1}^{k_N} P_x(t)_k \mathrm{e}^{-\frac{(x-b(t)_k)^2}{2{d_k}^2}}, \quad 0 \leq x \leq L \tag{47}$$

$$f_y(x, H, t) = \sum_{k=1}^{k_N} P_y(t)_k \mathrm{e}^{-\frac{(x-b(t)_k)^2}{2{d_k}^2}}, \quad 0 \leq x \leq L \tag{48}$$

where k_N denotes the number of the forces in motion; $P_x(t)_k$ and $P_y(t)_k$ denote the horizontal and vertical amplitudes at the peak location of the k-th force, respectively; $b(t)_k$ is the time-varying position of the peak of the k-th force; and d_k determines the horizontal width of the k-th force. The full width at a tenth of the maximum (FWTM), as illustrated in Figure 2, is employed to estimate the distribution width of the k-th load. It is related to d_k as follows:

$$d_k = \frac{\text{FWTM of the } k\text{-th force targeted}}{2\sqrt{2\ln 10}}. \tag{49}$$

In this study, the presented inversion method is tested using example cases in which a set of three (i.e., $k_N = 3$) targeted moving forces are exerted to the upper boundary of 2D solids with varied material properties. The three targeted moving loads (Loads A, B, and C) have vertical and horizontal components with spatial distributions, which vary in time, along the upper boundary where the FWTM of each load is 4.29 m ($d = 1.0$ m) as shown in Figs 4a and 4b. The horizontal component for each moving force has the same position and width of a central peak as its corresponding vertical one. Loads A, B, and C have different accelerations, initial velocities, initial positions, and amplitudes as shown below.

- The vertical component of force A is $P_y(t)_1 = -[400\sin(2\pi(15)t)+18000]$ N/m. Its horizontal counterpart is $P_x(t)_1 = -[400\sin(2\pi(15)t) + 5504.59 + (2700 + 1.225(25 + 3t)^2)]$ N/m. The x-location of the central peak for both $P_x(t)_1$ and $P_y(t)_1$ is $b(t)_1 = [8 + 25t + 0.5(3)t^2]$ m. Plugging $P_y(t)_1$, $P_x(t)_1$, and $b(t)_1$ into Eqs. (47) and (48) fully characterize Load A.
- Load B has $P_y(t)_2 = -[300\sin(2\pi(10)t) + 22000]$ N/m and $P_x(t)_2 = -[300\sin(2\pi(10)t) - 6727.83 - (3300 + 1.225(-30 - 3t)^2)]$ N/m with the central peak location $b(t)_2 = [33 - 30t - 0.5(3)t^2]$ m.
- Load C has $P_y(t)_3 = -[600\sin(2\pi(5)t) + 32000]$ N/m and $P_x(t)_3 = -[600\sin(2\pi(5)t) - 19571.9 + (4800 + 1.225(40 - 6t)^2)]$ N/m with the central peak location $b(t)_3 = [-45 - 40t - 0.5(6)t^2]$ m.

The time-varying amplitudes, $P_x(t)$ and $P_y(t)$, have static and dynamic components. When it comes to the identification of moving loads on a roadway, the static part of $P_y(t)$ may represent the weight of a vehicle while its dynamic part can model vertical forces such as those induced by the powertrain vibrations.

Assessment of the inversion error

To evaluate the inversion performance, the discrepancy between the guessed and targeted force is determined by the normalized mean absolute error equation:

$$\mathcal{E} = \frac{\sum_{n=1}^{N} \sum_{j=1}^{j_N} |f_{nj_{\text{target}}} - f_{nj_{\text{estimate}}}|}{\sum_{n=1}^{N} \sum_{j=1}^{j_N} |f_{nj_{\text{target}}}|}, \tag{50}$$

where $f_{nj_{\text{target}}}$ denotes a targeted nodal force at n-th timestep and j-th node that is resulted from the finite element approximation of the targeted traction in Eqs. (47) and (48). $f_{nj_{\text{estimate}}}$ denotes its estimated counterpart. It has been observed that the errors computed using the normalized mean absolute error equation (50) may have large values even when plots of the reconstructed loads visually compare well to plots of the target loads. Nonetheless, the normalized mean absolute error serves as a useful metric for assessing the progression of inversion results over iterations and for comparing results across various cases that share the same target loads.

Example 1: In-depth inspection of the performance of RK-based inversion and Newmark-based inversion

For Example 1, the accuracy of the RK-based inversion is compared to that of the Newmark-based inversion. Herein the three target moving loads are applied to a 2D solid that is 30 m wide and 10 m in height and is layered with two material layers representing multi-layered ground soil. In the initial test, Layer 1, at the upper part ($y = 5$ to 10 m) of the solid, consists of Material 1 listed in Table 1 with a damping constant of $\alpha = 2000$ kg/(m^3 s), and Layer 2, at the lower part ($y = 0$ to 5 m), consists of Material 2 in Table 1 with a damping constant of $\alpha = 2500$ kg/(m^3 s). $\Delta t = 0.002$ s is used for both the RK and Newmark-based models in Example 1. Using 1000 time steps, the forward models have a duration of 2 s. Based on the maximum wave speed in the problem, $v_{max} = 178.23$ m/s, and the minimum distance between nodes, $r_{min} = 0.5$ m, the CFL condition requires that $\Delta t_{max} = 0.00281$ s, which is met by Δt of 0.002 s. Sensors are spaced every three meters along the top surface of the solid.

First, the results of the forward model using the RK method and the Newmark method are compared. Figure 3 shows the displacements computed at the top center point on the rectangular solid, $(15, 10)$ m, by the forward model for the target loading using the Newmark method with no lumping of the mass matrix and the RK method with the lumped mass matrix. They are in excellent agreement with each other.

Figure 4 shows the contour plots of force in the x- and y-directions in space and time for the target and identified loads produced after 300 iterations by both the RK and Newmark inversions. Fig. 4 shows that, after 300 iterations, both the Newmark-based inversion and the RK-based inversion produce reconstructions of the loading that capture the number of loads, the changing positions and widths of the loads, and whether they are positively or negatively directed. In Example 1, the values of the error norm, $\mathcal{E}$, after 300 iterations are 0.73 for the Newmark inversion and 0.70 for the RK inversion.

Figure 5 shows the snapshots of the target loading compared with the identified one produced after 300 iterations using the RK-based inversion and the Newmark-based inversion at two different time steps. Figure 6 shows plots of the amplitude for the loading at all time steps at two points on the top surface, $(15, 10)$ m $(16.5, 10)$ m, for the duration of the simulation. The point $(15, 10)$ m is the location of one of the sensors, and the point $(16.5, 10)$ m is a point on the top surface midway between two sensors. While both inversion methods show a greater tendency to underestimate the amplitudes of the distributed loads at points the more distant they are from the sensors, the RK-based inversion tends to underestimate the loading even more than the Newmark-based inversion does. It should be considered that the force parameters in every half time step are inverted when the RK-based inversion is performed, while the Newmark inversion updates force parameters at every whole time step only. Thus, the control-variable space of the force inversion problem becomes larger for a given observation duration when the RK inversion is used than when the Newmark inversion is used. The more control parameters lead to stronger solution multiplicity. Namely, 122,000 parameters (=61 nodes on the top surface $\times$ 1,000 time steps $\times$ 2 (counting every half time steps) are inverted in the RK inversion in contrast to 61,000 parameters for the Newmark inversion. The tendency for the inverted force profile to underestimate the target profile more when we use the RK inversion than the Newmark inversion could be due to the increased solution multiplicity.

Overall, the results for the two inversion methods have many similarities to each other and predict the existence of the moving loads, their numbers, and their positions well. However, the average elapsed time per iteration for this example using the RK inversion is 15.81 s/iteration which is a 75.91 percent decrease from the 65.67 s/iteration average for the Newmark inversion. For all simulations in this paper, we used a desktop computer, of which CPU is 2.71 GHz, in a non-parallel mode on MATLAB.

To investigate the effect of material properties and damping on inversion results, the RK and Newmark-based inversion methods are tested for cases in which the solid is homogeneous with varying the material and damping conditions. The plots in Fig. 7 show that while the number of inversion iterations it takes for the change in error to become level off increases as the wave speeds increase (i.e., Material 2 vs 3) but decreases as the damping coefficient increases for both the RK and Newmark inversions. The comparison between the performance of the RK and Newmark inversions in Fig. 7 also shows that the accuracy of the RK inversion is close to the Newmark inversion regardless of the value of the damping coefficient of the solid.

As shown in Table 1, keeping the element size the same while increasing the wave speed of the material in the model may require decreasing the time step size in the RK method in order to satisfy the CFL condition. Decreasing the time step size for the RK inversion as the wave speeds in the example cases increase requires increasing the number of time steps in the model to model the same duration. Changing the time step size is not required when using the Newmark-based inversion method. Therefore, the number of parameters to invert each iteration may be greater using RK inversion than Newmark inversion for the same problem, and, when the wave speeds are sufficiently large, the elapsed times may be less for the Newmark inversion than the RK inversion method. Testing the inversion methods when the solid consists of different materials shows that, for a problem with the given number of degrees of freedom (DOFs), RK inversion is less time-consuming than Newmark inversion when the solid consists of Materials 1 to 3 but more time consuming than Newmark inversion when the solid consists of Material 4. However, there are other factors contributing to the elapsed time of the inversion. To clarify this aspect, Example 2 examines the relationship between the elapsed time of the RK and Newmark inversions and the number of DOFs in a problem.

Example 2: Elapsed time for RK and Newmark inversions

In Example 2, the moving loads are applied to rectangular homogeneous solids of varied sizes and for varied durations to test the RK and Newmark inversions, thus, changing the force-function discretization in both space and time. The solid consists of Material 1, and the time step size and the element size are $\Delta t = 0.002$ s and 1 m, respectively, in each case of Example 2. The sensors are spaced one every four meters. In Example 2, the RK and Newmark inversions reconstruct the sample moving loads with four different durations, 1 to 4 seconds, modeled using 500 to 2000 time steps, respectively. Eight different sizes of the domain are given to the solid, and their dimensions are listed in Table 2. The DOFs and time steps for each of the total 22 cases in Example 2 are listed in Table 2.

Figure 8 shows plots of the error given 300 inversion iterations using the RK inversion for a set of cases. Figure 8a shows the progress in terms of the inversion error for the RK inversion for four cases that have the same duration using the same number of time steps but differ with regard to the number of DOFs in the solid. Figure 8b shows how the RK inversion progresses for four cases, which have the same number of DOFs but differ with regard to the number of time steps with the same time step sizes. Figures 8a and 8b show that the increased DOFs and observation durations do not affect the inversion accuracy.

Additionally, increasing the DOFs leads to greater advantages in elapsed time for the RK inversion over the Newmark inversion. Figure 9a indicates that the elapsed time of the Newmark inversion increases with respect to the DOFs in the second order while that of the RK inversion grows in a linear fashion. Figure 9b shows that the elapsed time increases linearly with respect to increasing the number of time steps for both the RK and Newmark inversion methods. The plots in Fig. 9 present that the benefit of using the RK inversion, compared to the Newmark inversion, with respect to elapsed time significantly increases as the number of nodes increases in the problem and should be even more significant when 3D problems are considered. In Example 1, it was demonstrated that the RK method may require more time steps than the Newmark method if the RK model's time step size is smaller in order to ensure stability. However, as the spatial DOFs are increased, the elapsed time grows quadratically for the Newmark method while increasing the number of time steps when using the RK method only increases the elapsed time linearly making the RK inversion method preferable, even for problems that require more time steps, when the number of DOFs cause the Newmark inversion method to have very large run times.

Example 3: Performance of RK and Newmark-based inversions with respect to sensor spacing

To study the effect of sensor spacing, the RK inversion is examined for the same problem used in Example 1 but with an additional case where a sensor is positioned at every 1.5 meters instead of one sensor every three meters. The results show that decreasing the sensor spacing increases the inversion accuracy of our RK inversion. Figure 10a shows snapshots of horizontal and vertical components of the target loading and reconstructed loading produced after 300 iterations using the RK inversion when the sensors are spaced every three meters, as in Example 1, and when the sensors are spaced every one and a half meters. It shows that using a smaller sensor spacing, for the RK inversion, generally gives rise to an inverted force profile closer to the target profile. Figure 10b shows the error vs. iteration plots for the RK inversion when the sensors are spaced every three meters and when the sensors are spaced every one and half meters, and the error value is smaller for sensor spacing of 1.5 m than 3 m.

Example 4: The effect of noise in sensor data on the performance of the RK inversion

In the previous examples, the inversion takes perfect displacement data as input to reconstruct the applied moving sources. To test the RK inversion method when only imperfect data can be obtained, the problem presented in Example 1 is changed such that noise is added to the displacement data for each sensor in both $x-$ and $y-$ directions as follows:

$$u_{\mathrm{m}}^{\mathrm{noised}}(t) = u_{\mathrm{m}}(t) + A\ u_{\mathrm{m}}^{\mathrm{max}}\ \eta, \tag{51}$$

where A is an N-component-array of random numbers ranging from 0 to 1 with the normal distribution; $u_{\mathrm{m}}^{\mathrm{max}}$ is the maximum value of measured displacement u_{m} at the sensor for either x or y direction; and η is the noise level (e.g., $\eta = 0.05$ for 5% noise level). Alternatively for the introduction of noise, $u_{\mathrm{m}}^{\text{m-s}}$ may be used in Eq. (51) instead of $u_{\mathrm{m}}^{\mathrm{max}}$, where $u_{\mathrm{m}}^{\text{m-s}}$ denotes the mean square value of a signal $u_{\mathrm{m}}(t)$. Since the value of $u_{\mathrm{m}}^{\mathrm{max}}$ is larger than $u_{\mathrm{m}}^{\text{m-s}}$, using $u_{\mathrm{m}}^{\mathrm{max}}$ in Eq. (51) makes for a more severe condition at a given noise level than using $u_{\mathrm{m}}^{\text{m-s}}$.

The RK inversion method is tested given the case presented in Example 1 but with sensor data having noise levels of 2%, 5%, and 10%. Figure 11a shows that the error decreases in each case but the decrease in the error stalls earlier the greater the noise level is. The reconstructed loading tends to underestimate the target loading more when more noise is added which can be seen in Fig. 11b presenting the reconstructed forces in the $x-$ direction over time at a point on the upper boundary after 300 iterations for various noise level cases. Figs. 13a and 13b show the target forces in the $x-$ and $y-$ directions respectively while Figs. 13c and 13d show the reconstructed loading after 300 iterations given sensor data with 10% noise. Figure. 13 shows that although the error, when the sensor data noise level is 10%, does not diminish to the same extent that the error diminishes when noise is not introduced, the contour plot of the reconstructed loading still captures the number of moving sources applied as well as their directions, locations, and the timing of their movements.

Example 5: The effect of the uncertainty in a material property on the performance of the RK inversion

In all previous examples, the material properties in the problems are considered to be known for the purpose of inverse modeling. To test the RK inversion method when the uncertainty in a material property is introduced, the inversion is tested for the problem considered in Example 1 for various true material property values, shown in Table 1, while assuming in the inverse model that the solid is homogeneous and consists of Material 1.

- In Example 5, Case 5a gives a case in which the sensor data, used as input for the inversion, are the displacements produced by the target loading when the solid is homogeneous and consists of Material 1. The inverse model, then, assumes correctly that the solid is homogeneous and consists of Material 1. Case 5a presents a case without model error in modeling the solid material.
- In Case 5b, the sensor data are produced by the target loading when the solid is homogeneous and consists of Material 2. Since the inverse model assumes that the solid consists of Material 1, the error modeling v_p and v_s is 1.96% and -3.87% respectively.
- In Case 5c, the sensor data are produced by the target loading when the solid is homogeneous

and consists of Material 5. The inverse model, again, assumes that the solid consists of Material 1 and the error modeling v_p and v_s is -6.21% and -11.6% respectively.

The error plot in Fig. 12a compares the error over 300 iterations for Case 5a, Case 5b, and Case 5c. Increasing the discrepancies in the material properties leads to more error in the inversion results which can be seen in the amplitudes of the reconstructed forces plotted over time for various model error cases in Fig. 12b. Figs. 13e and 13f indicate that the reconstructed loading even for Case 5c after 300 iterations reconstructs the number of moving sources, their directions, their locations, and the timing of their movements well.

SUMMARY

As the core contribution of this paper, the DTO inversion formulation based on the RK forward time integration is fully described for the first time. The RK forward simulation is represented by a discrete forward operator, centered around the $\mathbf{Q}$ matrix, and its detail is fully disclosed in this paper. The forward operator is side-imposed into a minimization functional via the multiplication with an adjoint solution vector, and the formulation of the adjoint and control equations are detailed. Thus, experienced users can understand the formulation and implement it straightforwardly. The presented numerical scheme will be scalable to a wider array of inverse problems where the forward problems are resolved via the RK wave simulation.

The numerical experiments demonstrate the robustness of the RK-inversion in a 2D plane-strain solid. The force parameters are inverted for every half-time step when the RK-based inversion is performed while the Newmark inversion identifies those in every time step. As the spatial DOFs are increased, the elapsed time grows quadratically for the Newmark method while increasing the number of time steps when using the RK method only increases the elapsed time linearly making the RK inversion method preferable, even for problems that require more time steps, when the number of DOFs cause the Newmark inversion method to have very large run times. Thus, the RK-based source inversion is more efficient than the Newmark inversion when the number of DOFs becomes larger in problems. The increased DOFs and observation durations do not affect the inversion accuracy. Using a smaller sensor spacing, for the RK inversion, generally gives rise to an inverted force profile closer to the target profile. The presented inversion method can effectively identify the profiles of dynamic moving loads even when measurement data include noise or when the values of material properties are not accurately modeled in the inversion simulator.

The presented RK-DTO formulation can be easily extended into other inverse problems in 2D/3D settings, where various boundary conditions (e.g., truncated boundary) and material models (e.g., heterogeneity, anisotropy, and damping) are comprehensively modeled in the presented forward operator $\mathbf{Q}$ matrix, and the forward wave problems are solved by using the fourth-order RK explicit time integration.

APPENDIX I. ON THE DERIVATION OF $\mathbf{L}_1$ TO $\mathbf{L}_8$

To get the compact form of the RK method equations (26), first, the expressions for $\mathbf{k}_1$, $\mathbf{k}_2$, $\mathbf{k}_3$, and $\mathbf{k}_4$ are written in terms of $\bar{\mathbf{s}}_{n-1}$, $\bar{\mathbf{s}}_{n-1}$, $\bar{\mathbf{s}}_{n-0.5}$, and $\bar{\mathbf{s}}_n$ and substituted into the RK method equation (10). This results in a RK method equation (21) written in terms of $\bar{\mathbf{s}}_{n-1}$, $\bar{\mathbf{s}}_{n-1}$, $\bar{\mathbf{s}}_{n-0.5}$, and $\bar{\mathbf{s}}_n$ and then the compact form of the RK method (26). The expressions for $\mathbf{k}_1$, $\mathbf{k}_2$, $\mathbf{k}_3$, and $\mathbf{k}_4$ are written in terms of $\bar{\mathbf{s}}_{n-1}$, $\bar{\mathbf{s}}_{n-1}$, $\bar{\mathbf{s}}_{n-0.5}$, and $\bar{\mathbf{s}}_n$ the following way:

$$\mathbf{k}_1 = \frac{\partial \bar{\mathbf{s}}}{\partial t}\left(t_{n-1}, \bar{\mathbf{s}}_{n-1}\right) = \mathbf{J}\bar{\mathbf{s}}_{n-1} + \underline{\mathbf{M}}^{-1}\bar{\mathbf{f}}_{n-1}. \tag{I.1}$$

$$\begin{aligned}
\mathbf{k}_2 &= \frac{\partial \bar{\mathbf{s}}}{\partial t}\left(t_{n-1} + \frac{\Delta t}{2}, \bar{\mathbf{s}}_{n-1} + \frac{\Delta t}{2}\mathbf{k}_1\right) = \mathbf{J}\left(\bar{\mathbf{s}}_{n-1} + \frac{\Delta t}{2}\mathbf{k}_1\right) + \underline{\mathbf{M}}^{-1}\bar{\mathbf{f}}_{n-0.5} \\
&= \mathbf{J}\left[\bar{\mathbf{s}}_{n-1} + \frac{\Delta t}{2}\left(\mathbf{J}\bar{\mathbf{s}}_{n-1} + \underline{\mathbf{M}}^{-1}\bar{\mathbf{f}}_{n-1}\right)\right] + \underline{\mathbf{M}}^{-1}\bar{\mathbf{f}}_{n-0.5} \\
&= \mathbf{J}\left[\left(\mathbf{I} + \frac{\Delta t}{2}\mathbf{J}\right)\bar{\mathbf{s}}_{n-1} + \frac{\Delta t}{2}\underline{\mathbf{M}}^{-1}\bar{\mathbf{f}}_{n-1}\right] + \underline{\mathbf{M}}^{-1}\bar{\mathbf{f}}_{n-0.5} \\
&= \left(\mathbf{J} + \frac{\Delta t}{2}\mathbf{J}\mathbf{J}\right)\bar{\mathbf{s}}_{n-1} + \frac{\Delta t}{2}\mathbf{J}\underline{\mathbf{M}}^{-1}\bar{\mathbf{f}}_{n-1} + \underline{\mathbf{M}}^{-1}\bar{\mathbf{f}}_{n-0.5} \\
&= \mathbf{L}_1\bar{\mathbf{s}}_{n-1} + \mathbf{L}_2\underline{\mathbf{M}}^{-1}\bar{\mathbf{f}}_{n-1} + \underline{\mathbf{M}}^{-1}\bar{\mathbf{f}}_{n-0.5},
\end{aligned} \tag{I.2}$$

where

$$\mathbf{L}_1 = \mathbf{J} + \frac{\Delta t}{2}\mathbf{J}\mathbf{J} \text{ and } \mathbf{L}_2 = \frac{\Delta t}{2}\mathbf{J}. \tag{I.3}$$

$$\begin{aligned}
\mathbf{k}_3 &= \frac{\partial \bar{\mathbf{s}}}{\partial t}\left(t_{n-1} + \frac{\Delta t}{2}, \bar{\mathbf{s}}_{n-1} + \frac{\Delta t}{2}\mathbf{k}_2\right) = \mathbf{J}\left(\bar{\mathbf{s}}_{n-1} + \frac{\Delta t}{2}\mathbf{k}_2\right) + \underline{\mathbf{M}}^{-1}\bar{\mathbf{f}}_{n-0.5} \\
&= \mathbf{J}\left[\bar{\mathbf{s}}_{n-1} + \frac{\Delta t}{2}\left(\mathbf{L}_1\bar{\mathbf{s}}_{n-1} + \mathbf{L}_2\underline{\mathbf{M}}^{-1}\bar{\mathbf{f}}_{n-1} + \underline{\mathbf{M}}^{-1}\bar{\mathbf{f}}_{n-0.5}\right)\right] + \underline{\mathbf{M}}^{-1}\bar{\mathbf{f}}_{n-0.5} \\
&= \mathbf{J}\left[\left(\mathbf{I} + \frac{\Delta t}{2}\mathbf{L}_1\right)\bar{\mathbf{s}}_{n-1} + \frac{\Delta t}{2}\mathbf{L}_2\underline{\mathbf{M}}^{-1}\bar{\mathbf{f}}_{n-1} + \frac{\Delta t}{2}\underline{\mathbf{M}}^{-1}\bar{\mathbf{f}}_{n-0.5}\right] + \underline{\mathbf{M}}^{-1}\bar{\mathbf{f}}_{n-0.5} \\
&= \left(\mathbf{J} + \frac{\Delta t}{2}\mathbf{J}\mathbf{L}_1\right)\bar{\mathbf{s}}_{n-1} + \frac{\Delta t}{2}\mathbf{J}\mathbf{L}_2\underline{\mathbf{M}}^{-1}\bar{\mathbf{f}}_{n-1} + \frac{\Delta t}{2}\mathbf{J}\underline{\mathbf{M}}^{-1}\bar{\mathbf{f}}_{n-0.5} + \underline{\mathbf{M}}^{-1}\bar{\mathbf{f}}_{n-0.5} \\
&= \left(\mathbf{J} + \frac{\Delta t}{2}\mathbf{J}\mathbf{L}_1\right)\bar{\mathbf{s}}_{n-1} + \frac{\Delta t}{2}\mathbf{J}\mathbf{L}_2\underline{\mathbf{M}}^{-1}\bar{\mathbf{f}}_{n-1} + \left(\frac{\Delta t}{2}\mathbf{J} + \mathbf{I}\right)\underline{\mathbf{M}}^{-1}\bar{\mathbf{f}}_{n-0.5} \\
&= \mathbf{L}_3\bar{\mathbf{s}}_{n-1} + \mathbf{L}_4\underline{\mathbf{M}}^{-1}\bar{\mathbf{f}}_{n-1} + \mathbf{L}_5\underline{\mathbf{M}}^{-1}\bar{\mathbf{f}}_{n-0.5},
\end{aligned} \tag{I.4}$$

where

$$\mathbf{L}_3 = \mathbf{J} + \frac{\Delta t}{2}\mathbf{J}\mathbf{L}_1, \ \mathbf{L}_4 = \frac{\Delta t}{2}\mathbf{J}\mathbf{L}_2, \ \text{and } \mathbf{L}_5 = \frac{\Delta t}{2}\mathbf{J} + \mathbf{I}. \tag{I.5}$$

$$\begin{aligned}
\mathbf{k}_4 &= \frac{\partial \overline{\mathbf{s}}}{\partial t}\left(t_n, \overline{\mathbf{s}}_{n-1} + \Delta t \mathbf{k}_3\right) = \mathbf{J}\left(\overline{\mathbf{s}}_{n-1} + \Delta t \mathbf{k}_3\right) + \underline{\mathbf{M}}^{-1}\overline{\mathbf{f}}_n \\
&= \mathbf{J}\left[\overline{\mathbf{s}}_{n-1} + \Delta t\left(\mathbf{L}_3\overline{\mathbf{s}}_{n-1} + \mathbf{L}_4\underline{\mathbf{M}}^{-1}\overline{\mathbf{f}}_{n-1} + \mathbf{L}_5\underline{\mathbf{M}}^{-1}\overline{\mathbf{f}}_{n-0.5}\right)\right] + \underline{\mathbf{M}}^{-1}\overline{\mathbf{f}}_n \\
&= \mathbf{J}\left[\left(\mathbf{I} + \Delta t \mathbf{L}_3\right)\overline{\mathbf{s}}_{n-1} + \Delta t \mathbf{L}_4\underline{\mathbf{M}}^{-1}\overline{\mathbf{f}}_{n-1} + \Delta t \mathbf{L}_5\underline{\mathbf{M}}^{-1}\overline{\mathbf{f}}_{n-0.5}\right] + \underline{\mathbf{M}}^{-1}\overline{\mathbf{f}}_n \\
&= \left(\mathbf{J} + \Delta t \mathbf{J}\mathbf{L}_3\right)\overline{\mathbf{s}}_{n-1} + \Delta t \mathbf{J}\mathbf{L}_4\underline{\mathbf{M}}^{-1}\overline{\mathbf{f}}_{n-1} + \Delta t \mathbf{J}\mathbf{L}_5\underline{\mathbf{M}}^{-1}\overline{\mathbf{f}}_{n-0.5} + \underline{\mathbf{M}}^{-1}\overline{\mathbf{f}}_n \\
&= \mathbf{L}_6\overline{\mathbf{s}}_{n-1} + \mathbf{L}_7\underline{\mathbf{M}}^{-1}\overline{\mathbf{f}}_{n-1} + \mathbf{L}_8\underline{\mathbf{M}}^{-1}\overline{\mathbf{f}}_{n-0.5} + \underline{\mathbf{M}}^{-1}\overline{\mathbf{f}}_n,
\end{aligned} \tag{I.6}$$

where

$$\mathbf{L}_6 = \mathbf{J} + \Delta t \mathbf{J}\mathbf{L}_3, \ \mathbf{L}_7 = \Delta t \mathbf{J}\mathbf{L}_4, \ \text{and } \mathbf{L}_8 = \Delta t \mathbf{J}\mathbf{L}_5. \tag{I.7}$$

DATA AVAILABILITY

Some or all data, models, or code generated or used during the study are available from the corresponding author by request.

- MATLAB code (.m format) of the simulations.
- MATLAB datasets (.mat format) of the simulation data.

ACKNOWLEDGMENT

This material is based upon work supported by the National Science Foundation under Award CMMI-2044887 and CMMI-2053694. Any opinions, findings, and conclusions or recommendations expressed in this material are those of the authors and do not necessarily reflect the views of the National Science Foundation. The authors are also grateful for the support by the Faculty Research and Creative Endeavors (FRCE) Research Grant-48058 at Central Michigan University. The authors appreciate the reviewers for their reviews and insightful comments.

REFERENCES

Aguiló, M., Aquino, W., Brigham, J. C., Fatemi, M., et al. (2010). "An inverse problem approach for elasticity imaging through vibroacoustics." *Medical Imaging, IEEE Transactions on*, 29(4), 1012–1021.

Aloisio, A., Rosso, M. M., and Alaggio, R. (2022). "Experimental and analytical investigation into the effect of ballasted track on the dynamic response of railway bridges under moving loads." *Journal of Bridge Engineering*, 27(10).

Aquino, W., Bunting, G., Miller, S. T., and Walsh, T. F. (2019). "A gradient-based optimization approach for the detection of partially connected surfaces using vibration tests." *Computer Methods in Applied Mechanics and Engineering*, 345, 323 – 335.

Askan, A., Akcelik, V., Bielak, J., and Ghattas, O. (2007). "Full Waveform Inversion for Seismic Velocity and Anelastic Losses in Heterogeneous Structures." *Bulletin of the Seismological Society of America*, 97(6), 1990–2008.

Au, F., Jiang, R., and Cheung, Y. (2004). "Parameter identification of vehicles moving on continuous bridges." *Journal of Sound and Vibration*, 269(1), 91–111.

Chatzi, E. N., Hiriyur, B., Waisman, H., and Smyth, A. W. (2011). "Experimental application and enhancement of the XFEM–GA algorithm for the detection of flaws in structures." *Computers & Structures*, 89(7), 556–570.

Daley, T. M., Freifeld, B. M., Ajo-Franklin, J., Dou, S., Pevzner, R., Shulakova, V., Kashikar, S., Miller, D. E., Goetz, J., Henninges, J., et al. (2013). "Field testing of fiber-optic distributed acoustic sensing (das) for subsurface seismic monitoring." *The Leading Edge*, 32(6), 699–706.

Ding, H., Chen, L.-Q., and Yang, S.-P. (2012). "Convergence of galerkin truncation for dynamic response of finite beams on nonlinear foundations under a moving load." *Journal of Sound and Vibration*, 331(10), 2426–2442.

Fathi, A., Poursartip, B., and Kallivokas, L. F. (2015). "Time-domain hybrid formulations for wave simulations in three-dimensional PML-truncated heterogeneous media." *International Journal for Numerical Methods in Engineering*, 101(3), 165–198.

Ghahari, S., Abazarsa, F., Jeong, C., Kurtulus, A., and Taciroglu, E. (2018a). "Blind identification of site effects and bedrock motion from surface response signals." *Soil Dynamics and Earthquake

Engineering, 107, 322 – 331.

Ghahari, S., Abazarsa, F., and Taciroglu, E. (2018b). "Probabilistic blind identification of site effects from ground surface signals." *Bulletin of Earthquake Engineering*, 16, 1079–1104.

Guidio, B. and Jeong, C. (2021a). "Full-waveform inversion of incoherent dynamic traction in a bounded 2D domain of scalar wave motions." *Journal of Engineering Mechanics*, 147.

Guidio, B. and Jeong, C. (2021b). "On the feasibility of simultaneous identification of a material property of a timoshenko beam and a moving vibration source." *Engineering Structures*, 227, 111346.

Guidio, B., Jeremić, B., Guidio, L., and Jeong, C. (2022). "Passive seismic inversion of SH wave input motions in a truncated domain." *Soil Dynamics and Earthquake Engineering*, 158, 107263.

Guzina, B. B., Fata, S. N., and Bonnet, M. (2003). "On the stress-wave imaging of cavities in a semi-infinite solid." *International Journal of Solids and Structures*, 40(6), 1505–1523.

Jeong, C., Peixoto, A. C. S., Aquino, A., Lloyd, S., and Arhin, S. (2017). "Genetic algorithm-based acoustic-source inversion approach to detect multiple moving wave sources of an arbitrary number." *Journal of Computing in Civil Engineering*, 31(5), 04017020.

Jeong, C. and Seylabi, E. E. (2018). "Seismic input motion identification in a heterogeneous halfspace." *Journal of Engineering Mechanics*, 144(8), 04018070.

Jiang, R., Au, F., and Cheung, Y. (2003). "Identification of masses moving on multi-span beams based on a genetic algorithm." *Computers and Structures*, 81(22), 2137–2148.

Jung, J., Jeong, C., and Taciroglu, E. (2013). "Identification of a scatterer embedded in elastic heterogeneous media using dynamic XFEM." *Computer Methods in Applied Mechanics and Engineering*, 259, 50–63.

Jung, J. and Taciroglu, E. (2014). "Modeling and identification of an arbitrarily shaped scatterer using dynamic XFEM with cubic splines." *Computer Methods in Applied Mechanics and Engineering*, 278, 101–118.

Jung, J. and Taciroglu, E. (2016). "A divide-alternate-and-conquer approach for localization and shape identification of multiple scatters in heterogeneous media using dynamic XFEM." *Inverse Problems and Imaging*, 10(1).

Kallivokas, L. F., Fathi, A., Kucukcoban, S., Stokoe, K. H., Bielak, J., and Ghattas, O. (2013). "Site characterization using full waveform inversion." *Soil Dynamics and Earthquake Engineering*, 47, 62–82.

Kang, J. W. and Kallivokas, L. F. (2010). "The inverse medium problem in 1D PML-truncated heterogeneous semi-infinite domains." *Inverse Problems in Science and Engineering*, 18(6), 759–786.

Komatitsch, D. and Tromp, J. (1999). "Introduction to the spectral element method for three-dimensional seismic wave propagation." *Geophysical Journal International*, 139(3), 806–822.

Kucukcoban, S. and Kallivokas, L. F. (2011). "Mixed perfectly-matched-layers for direct transient analysis in 2D elastic heterogeneous media." *Computer Methods in Applied Mechanics and Engineering*, 200, 57–76.

Lee, J. H. (2023). "Consistent transmitting boundaries for time-domain analyses of wave propagation in layered anisotropic waveguides." *International Journal for Numerical Methods in Engineering*, 124(8), 1883–1907.

Lin, Y.-H. and Trethewey, M. W. (1990). "Finite element analysis of elastic beams subjected to moving dynamic loads." *Journal of Sound and Vibration*, 136(2), 323–342.

Lloyd, F. and Jeong, C. (2018). "Adjoint equation-based inverse-source modeling to reconstruct moving acoustic sources in a 1D heterogeneous solid." *Journal of Engineering Mechanics*, 144(9), 04018089.

Lloyd, S. and Jeong, C. (2022). "Identifying moving vibrational sources in a truncated, damped, heterogeneous solid." *International Journal of Computational Methods*, 20(1), 2250030.

Lloyd, S., Schaal, C., and Jeong, C. (2023). "Inverse modeling and experimental validation for reconstructing wave sources on a 2d solid from surficial measurement." *Ultrasonics*, 128, 106880.

Ngeljaratan, L. and Moustafa, M. A. (2020). "Structural health monitoring and seismic response assessment of bridge structures using target-tracking digital image correlation." *Engineering Structures*, 213, 110551.

Ni, F., Zhang, J., and Taciroglu, E. (2023). "Development of a moving vehicle identification framework using structural vibration response and deep learning algorithms." *Mechanical Systems and Signal Processing*, 201, 110667.

Oh, S., uk Ahn, C., Ahn, K., and Kim, J.-G. (2023). "Implicit inverse force identification method for vibroacoustic finite element model." *Journal of Sound and Vibration*, 117713.

Pakravan, A., Kang, J. W., and Newtson, C. M. (2016). "A Gauss-Newton full-waveform inversion for material profile reconstruction in viscoelastic semi-infinite solid media." *Inverse Problems in Science and Engineering*, 24(3), 393–421.

Raftoyiannis, I. G., Avraam, T. P., and Michaltsos, G. T. (2014). "Analytical models of floating bridges under moving loads." *Engineering Structures*, 68, 144–154.

Tromp, J., Komattisch, D., and Liu, Q. (2008). "Spectral-element and adjoint methods in seismology." *Communications in Computational Physics*, 3(1), 1–32.

Walsh, T., Aquino, W., and Ross, M. (2013). "Source Identification in Acoustics and Structural Mechanics using SIERRA/SD." *Report no.*, Sandia National Laboratories, <https://prod-ng.sandia.gov/techlib-noauth/access-control.cgi/2013/132689.pdf>.

List of Tables

1 Material properties and related RK method's maximum allowable time step conditions ($r_{min} = 0.5$ m). 35

2 Example 2: Domain dimensions for cases. 36

TABLE 1. Material properties and related RK method's maximum allowable time step conditions ($r_{min} = 0.5$ m).

Material	E (GPa)	ρ (kg/m^3)	ν	v_p (m/s)	v_s (m/s)	Δt_{max} (s)
Material 1	0.045	1,700	0.25	178.23	102.90	0.00281
Material 2	0.055	2,000	0.20	174.80	107.04	0.00286
Material 3	0.550	2,000	0.20	552.77	338.50	0.00091
Material 4	2.500	2,000	0.20	1178.51	721.69	0.00042
Material 5	0.065	2,000	0.20	190.03	116.37	0.00263

TABLE 2. Example 2: Domain dimensions for cases.

Size	Width (m)	Height (m)	Horizontal nodes	Vertical nodes	Spatial nodes	DOF	Number of time steps
Size 1	8	7	17	15	255	510	500, 1500
Size 2	8	8	17	17	289	578	500, 1000, 1500, 2000
Size 3	8	9	17	19	323	646	500, 1500
Size 4	8	10	17	21	357	714	500, 1500
Size 5	8	11	17	23	391	782	500, 1500
Size 6	16	16	33	33	1089	2178	500, 1000, 1500, 2000
Size 7	24	24	49	49	2401	4802	500, 1000, 1500, 2000
Size 8	32	32	65	65	4225	8450	500, 1500

List of Figures

1 A stratified solid subjected to a dynamic distributed load in motion on its upper surface. The lower boundary of the solid is immovably fixed, and wave movements are recorded at an upper boundary. 39

2 A distributed moving or stationary traction. FWTM denotes the full width at a tenth of the maximum force amplitude. 40

3 Example 1: Displacement vs. time plots for displacements computed by the forward model at point (15,10) m for the target loading using the Newmark method and the RK method: (a) u_x and (b) u_y. 41

4 Example 1: (a) and (b) the target forces in the x and y directions; (c) and (d) the inverted counterparts using the Newmark method; (e) and (f) the inverted counterparts using the RK method. 42

5 Example 1: The target and inverted loads in the x and y directions at (a) $t = 0.5$ s and (b) $t = 1.5$ s after 300 iterations. 43

6 Example 1: The target and predicted force over time at (a) $(15, 10)$ m, a surficial point where there is a sensor, and (b) $(16.5, 10)$ m, a surficial point midway between two neighboring sensors, after 300 iterations. 44

7 Example 1: Error vs. iteration plots comparing the effects of damping on performance when using the RK and Newmark inversions: (a) Material 2 and (b) Material 3. 45

8 Example 2: Sample error vs. iteration plots for the RK inversion for 300 iterations including (a) error plotted for four cases with the same number of time steps but increasing spatial DOFs, and (b) error plotted for four cases with the same DOFs but increasing duration leading to more time steps. . . 46

9 Example 2: Plots of elapsed time as the number of parameters change specifically (a) elapsed time vs. DOFs for cases with 500 and 1500 time steps in the model and (b) elapsed time vs. the total number of time steps for cases with 578, 2178, and 4802 DOFs. 47

10 Example 3: The performance of the RK inversion with respect to the sensor spacing (a) Snapshot of $x-$ and $y-$components for the targeted and inverted loads at $t = 1.68$ s after 300 iterations. (b) Error vs. iteration up to 300 iterations. 48

11 Example 4: Results of tests on the effect of noise in the sensor data on RK inversion outcomes including (a) error plotted for cases with various noise levels, and (b) the reconstructed force in the $x-$ direction at a point on the upper boundary, (15, 10) m, at 300 iterations for various noise levels. 49

12 Example 5: Results of tests on the effect of material property value's uncertainty on RK inversion outcomes including (a) error plotted for various cases of material property value's uncertainties, and (b) the reconstructed force in the $x-$ direction at a point on the upper boundary, (15, 10) m, at 300 iterations for the cases. 50

13 Examples 4 and 5: (a) and (b) the target forces in the x and y directions; (c) and (d) the inverted forces after 300 iterations using the RK inversion method with 10% noise introduced in the measurement input in Example 4; (e) and (f) the inverted forces after 300 iterations using the RK inversion method for Case 5b with material property value's uncertainty. 51

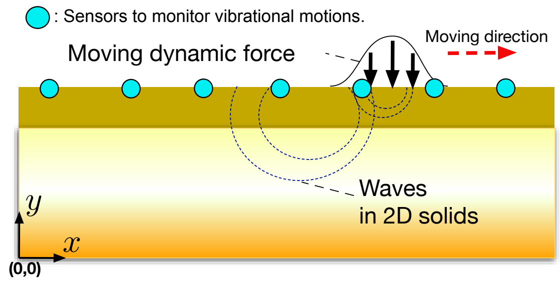

Fig. 1. A stratified solid subjected to a dynamic distributed load in motion on its upper surface. The lower boundary of the solid is immovably fixed, and wave movements are recorded at an upper boundary.

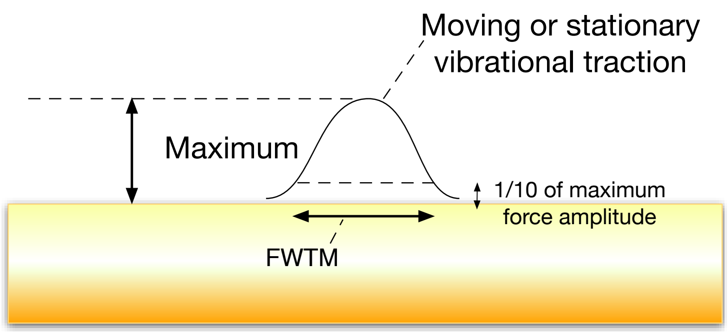

Fig. 2. A distributed moving or stationary traction. FWTM denotes the full width at a tenth of the maximum force amplitude.

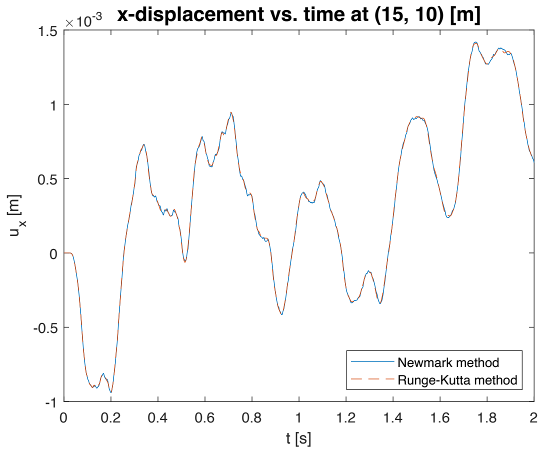

(a)

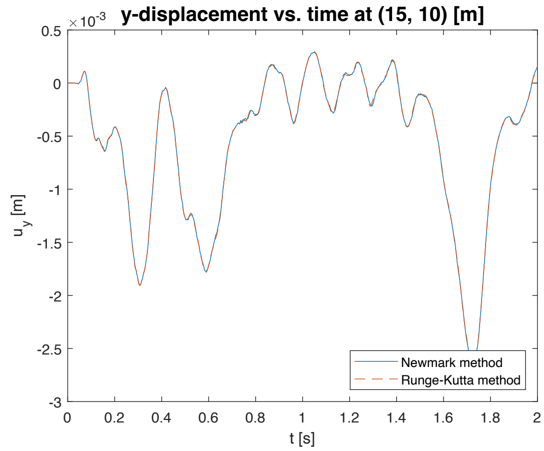

(b)

Fig. 3. Example 1: Displacement vs. time plots for displacements computed by the forward model at point (15,10) m for the target loading using the Newmark method and the RK method: (a) u_x and (b) u_y.

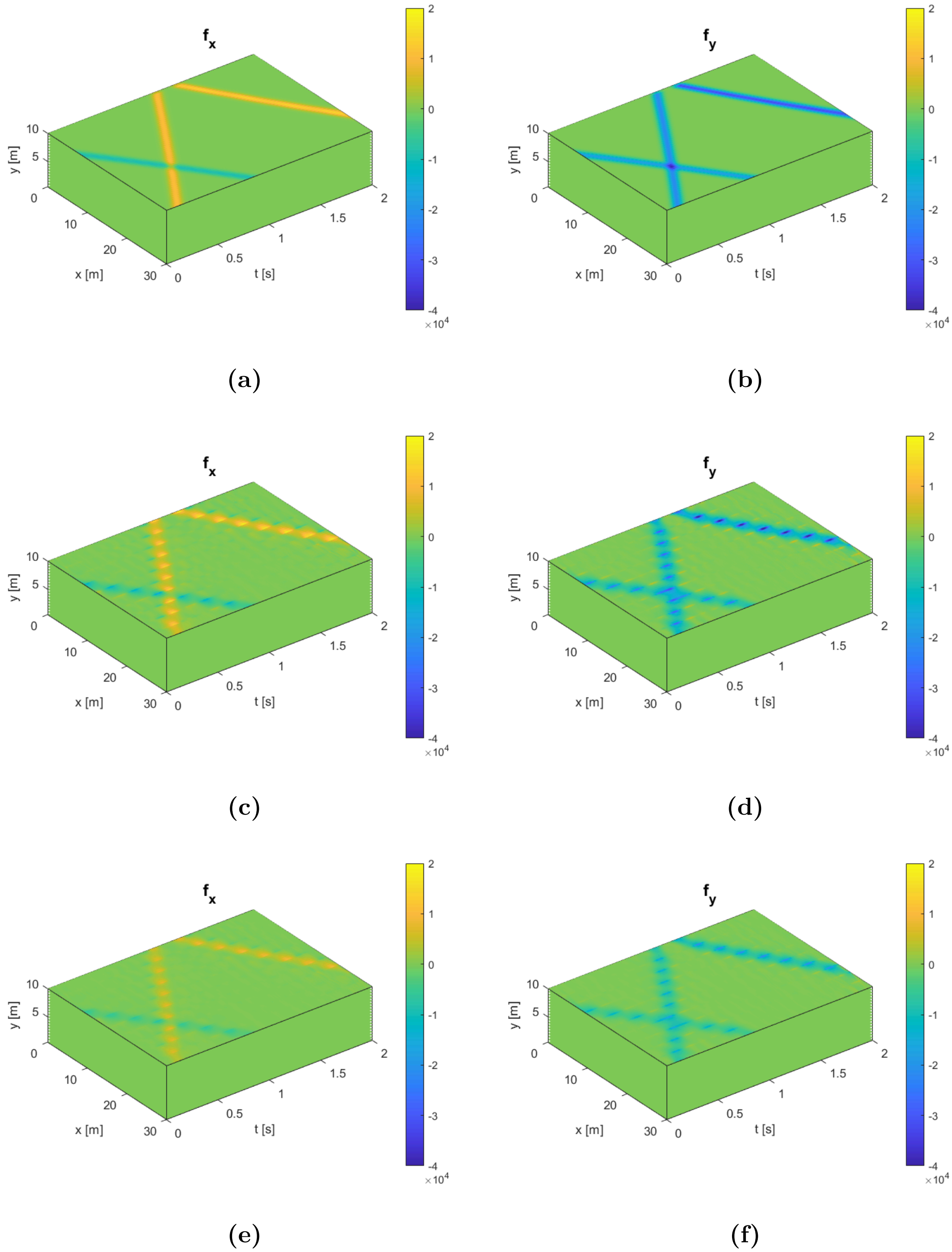

Fig. 4. Example 1: (a) and (b) the target forces in the x and y directions; (c) and (d) the inverted counterparts using the Newmark method; (e) and (f) the inverted counterparts using the RK method.

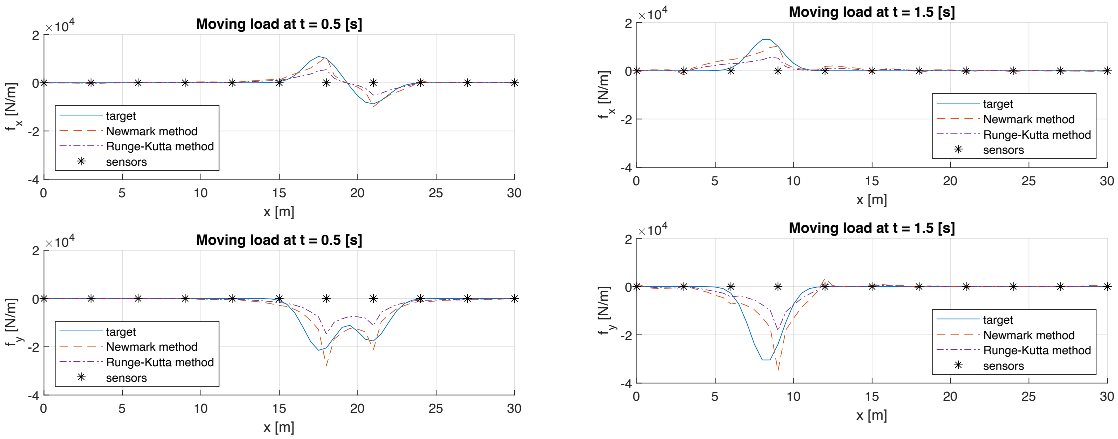

(a) **(b)**

Fig. 5. Example 1: The target and inverted loads in the x and y directions at (a) $t = 0.5$ s and (b) $t = 1.5$ s after 300 iterations.

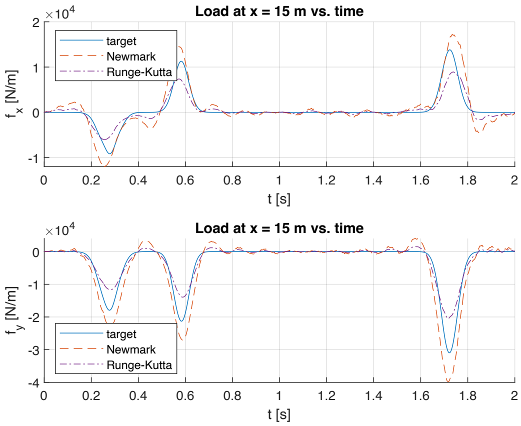

(a)

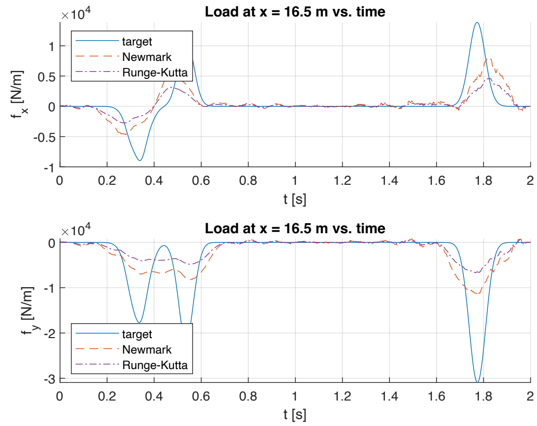

(b)

Fig. 6. Example 1: The target and predicted force over time at (a) $(15, 10)$ m, a surficial point where there is a sensor, and (b) $(16.5, 10)$ m, a surficial point midway between two neighboring sensors, after 300 iterations.

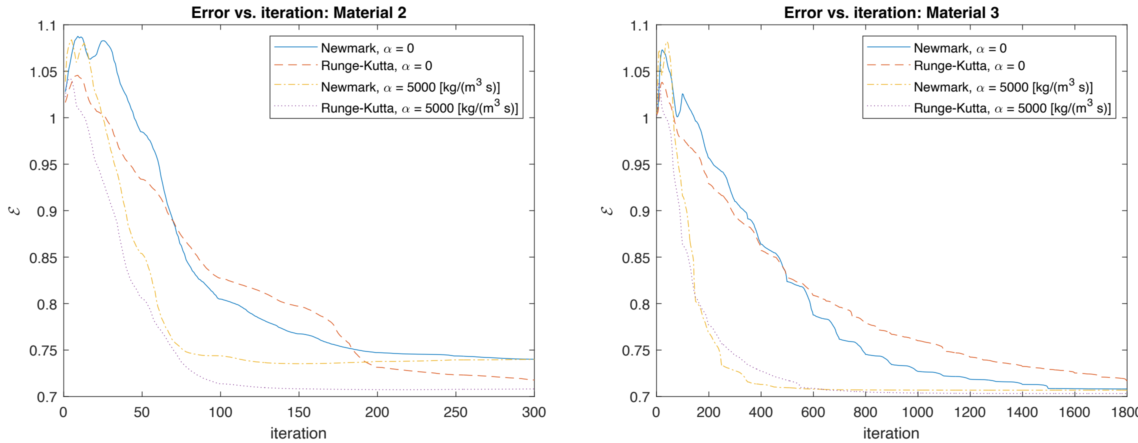

(a) **(b)**

Fig. 7. Example 1: Error vs. iteration plots comparing the effects of damping on performance when using the RK and Newmark inversions: (a) Material 2 and (b) Material 3.

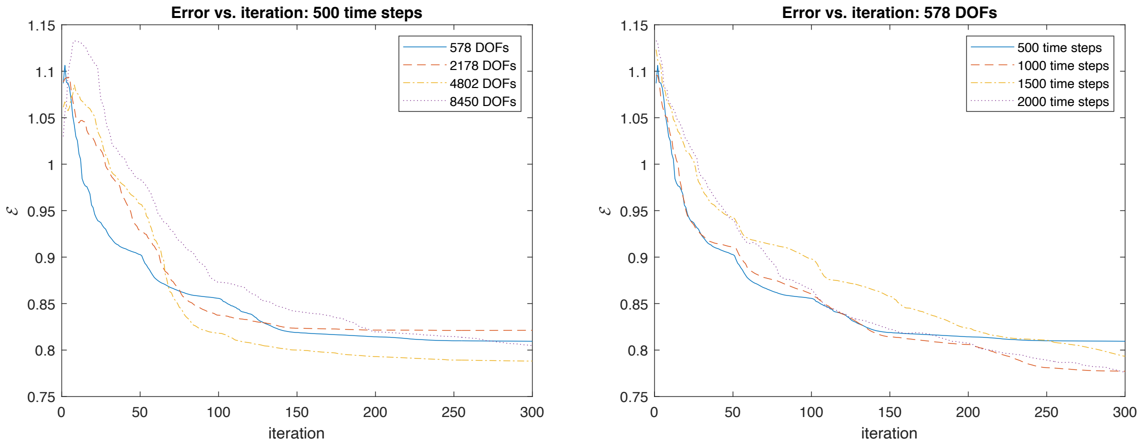

(a) **(b)**

Fig. 8. Example 2: Sample error vs. iteration plots for the RK inversion for 300 iterations including (a) error plotted for four cases with the same number of time steps but increasing spatial DOFs, and (b) error plotted for four cases with the same DOFs but increasing duration leading to more time steps.

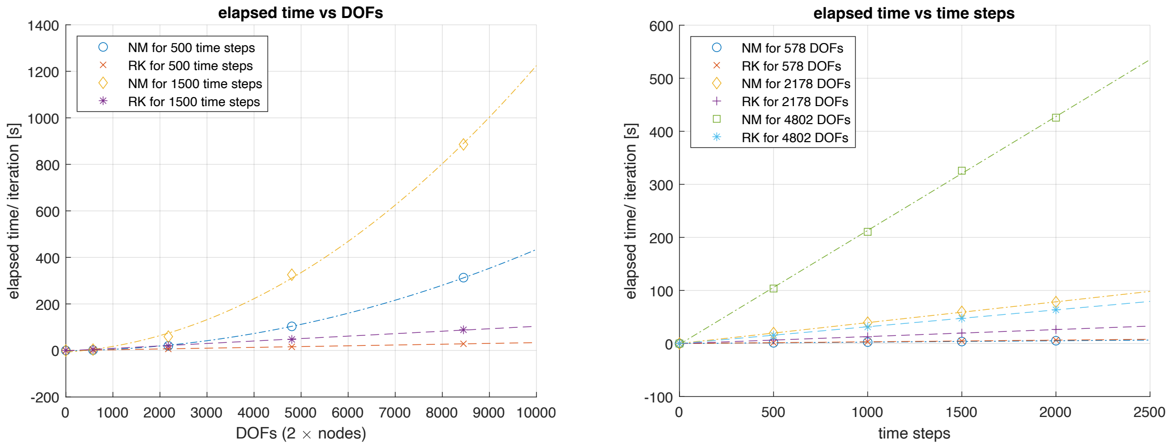

(a) **(b)**

Fig. 9. Example 2: Plots of elapsed time as the number of parameters change specifically (a) elapsed time vs. DOFs for cases with 500 and 1500 time steps in the model and (b) elapsed time vs. the total number of time steps for cases with 578, 2178, and 4802 DOFs.

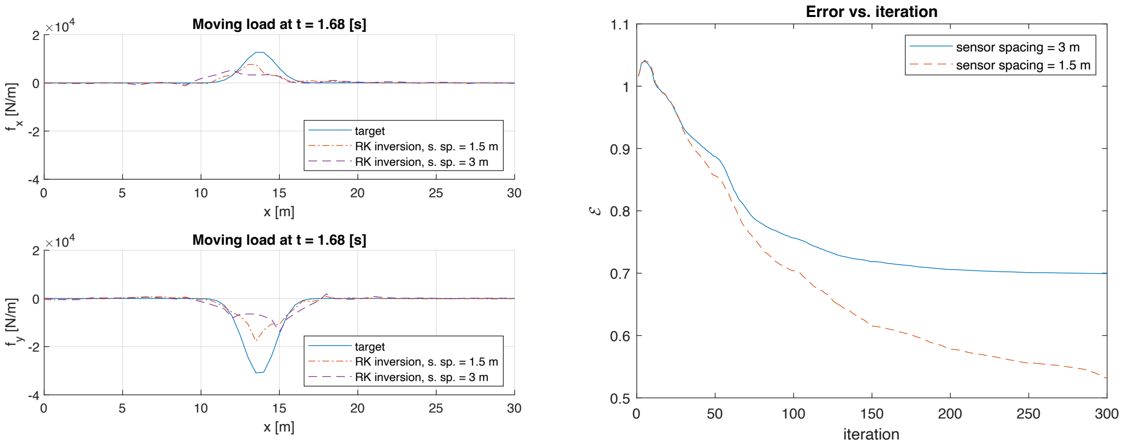

(a) **(b)**

Fig. 10. Example 3: The performance of the RK inversion with respect to the sensor spacing (a) Snapshot of $x-$ and $y-$components for the targeted and inverted loads at $t = 1.68$ s after 300 iterations. (b) Error vs. iteration up to 300 iterations.

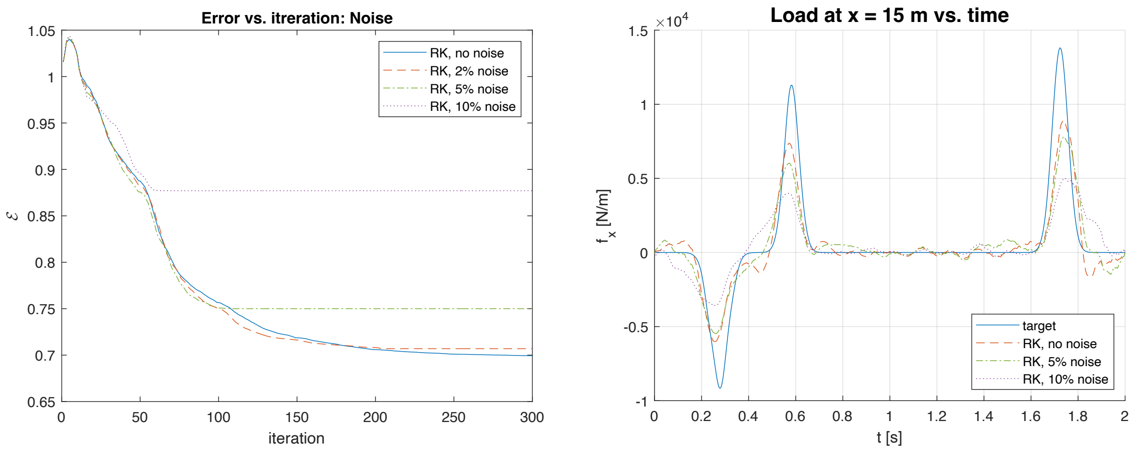

(a) **(b)**

Fig. 11. Example 4: Results of tests on the effect of noise in the sensor data on RK inversion outcomes including (a) error plotted for cases with various noise levels, and (b) the reconstructed force in the $x-$ direction at a point on the upper boundary, (15, 10) m, at 300 iterations for various noise levels.

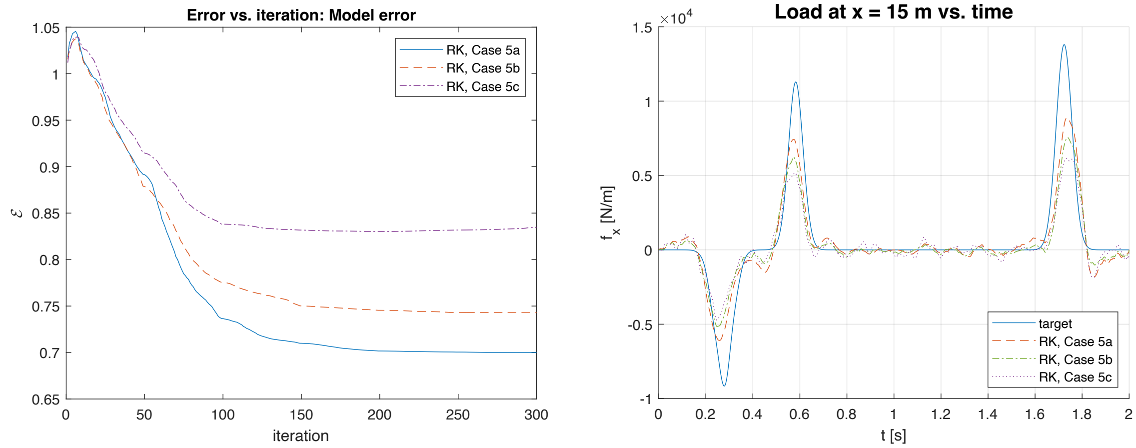

(a) **(b)**

Fig. 12. Example 5: Results of tests on the effect of material property value's uncertainty on RK inversion outcomes including (a) error plotted for various cases of material property value's uncertainties, and (b) the reconstructed force in the $x-$ direction at a point on the upper boundary, (15, 10) m, at 300 iterations for the cases.

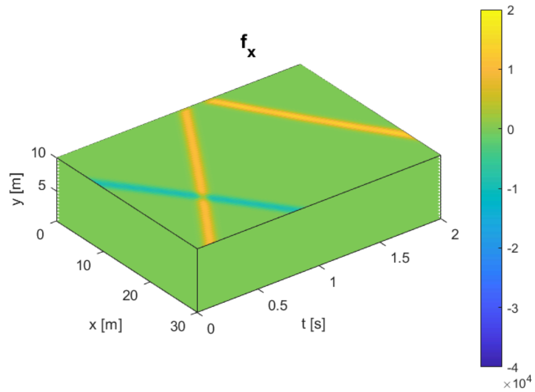

(a)

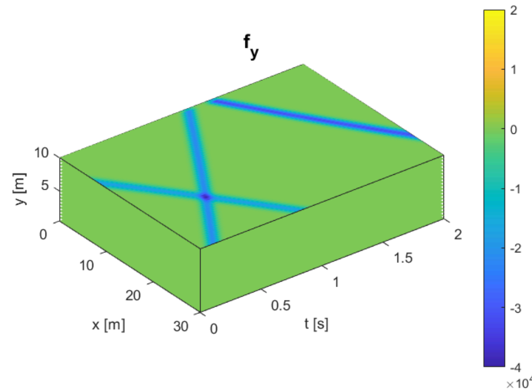

(b)

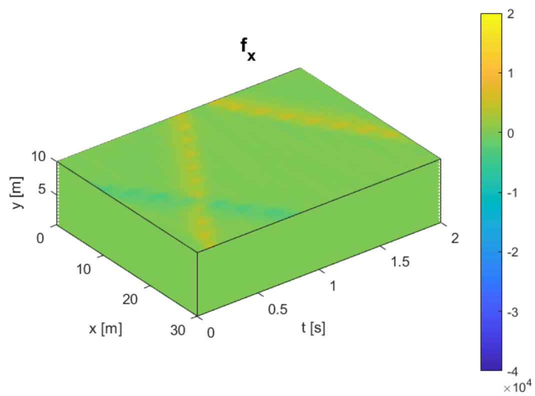

(c)

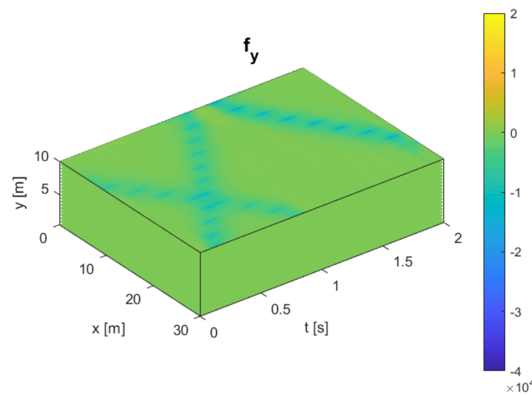

(d)

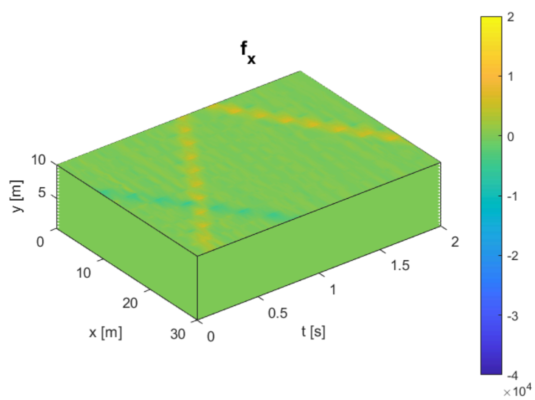

(e)

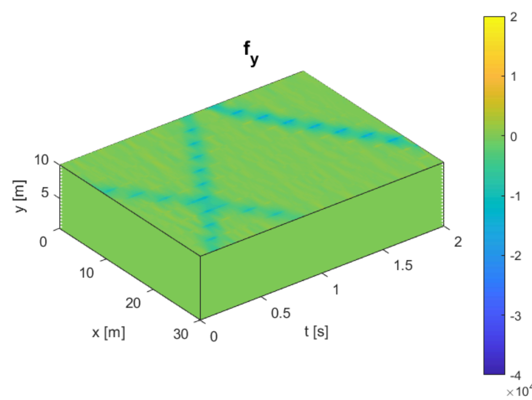

(f)

Fig. 13. Examples 4 and 5: (a) and (b) the target forces in the x and y directions; (c) and (d) the inverted forces after 300 iterations using the RK inversion method with 10% noise introduced in the measurement input in Example 4; (e) and (f) the inverted forces after 300 iterations using the RK inversion method for Case 5b with material property value's uncertainty.